Article:
Wang, Y., Wignall, P.B., Mills, B.J.W. et al. (Accepted: 2026) Cooling-induced intensification of ocean anoxia in the mid-Paleozoic. Science Advances. ISSN: 2375-2548 (In Press)

Science Advances
AAAS

Supplementary Materials for

Cooling-induced intensification of ocean anoxia in the mid-Paleozoic

Yuxuan Wang *et al.*

*Corresponding author. Email: Yuxuan Wang (wyxleeds@gmail.com); Paul Wignall (p.b.wignall@leeds.ac.uk); Simon Poulton (s.poulton@leeds.ac.uk)

This PDF file includes:

Supplementary Text

Geological background and sample description

The Ireviken extinction event (IEE)

The mid-Silurian Ireviken Extinction Event (IEE) straddles the Telychian and Sheinwoodian Stage boundary, and lasted more than 0.7 Ma (Fig. 4). A significant conodont extinction in the late Telychian *(1,2)* saw the loss of 48 out of 60 pandemic species, representing an extinction rate of 80%, and conodont diversity did not fully recover for the remainder of the Silurian *(3)*. A major phase of graptolite decline, with species diversity declining from 21 to 4, occurred in the early Sheinwoodian *(4,5)*. Other marine taxa, including chitinozoans, ostracods, corals and trilobites, also experienced significant crises to varying extents at various times *(6)*.

The early Sheinwoodian carbon isotope (ESCIE)

Although the magnitude of carbon isotope excursions varies and may be influenced by local or regional depositional conditions, the Early Sheinwoodian Carbon Isotope Excursion (ESCIE) has been globally documented across diverse sedimentary facies from different paleocontinents *(1,7)* (Fig. S1A). Most ESCIE records are derived from shallow-water carbonate platforms, with the highest $\delta^{13}C_{carb}$ values of 6.6‰ being reported from Norway *(8)*, with ~5.5‰ peaks in New York State and Ontario *(9)*, 5‰ in Sweden *(10)* (Gotland), 4‰ in Oklahoma, and 3‰ in Nevada *(11)*. In stratigraphic sections with well-defined graptolite biostratigraphy, such as the Baltic cores *(12,13)* and the Aizpute-41 section in Latvia *(14)*, the onset of the ESCIE occurs in the late *murchisoni* Biozone in the later stages or slightly after the IEE *(1)*. Peak $\delta^{13}C_{carb}$ values are observed within the *riccartonensis* Biozone or

slightly higher. In deeper-water graptolitic facies of the Baltoscandian Basin, the $\delta^{13}C$ excursion begins in the upper *murchisoni* Biozone and concludes in the Middle Wenlock *(15)*. Notably, the peak interval of the ESCIE shows a significant temporal offset from the main phase of the IEE.

In the UK, the Early Sheinwoodian Carbon Isotope Excursion (ESCIE) is well-documented across different depositional settings, from the inner shelf Midland carbonate platform (Eastnor Park and Lower Hill Farm boreholes *(15)*) to the mid and outer clastic shelf (Buttington section *(17)* and Banwy River section *(12)*, respectively) and into the deep basin at the Ashgill Beck section (Fig. S1B). On the shallow Midland carbonate platform, the EP and LHM boreholes record a maximum $\delta^{13}C_{carb}$ increase of over 4‰, initiating in the early Sheinwoodian (Fig. S1C).

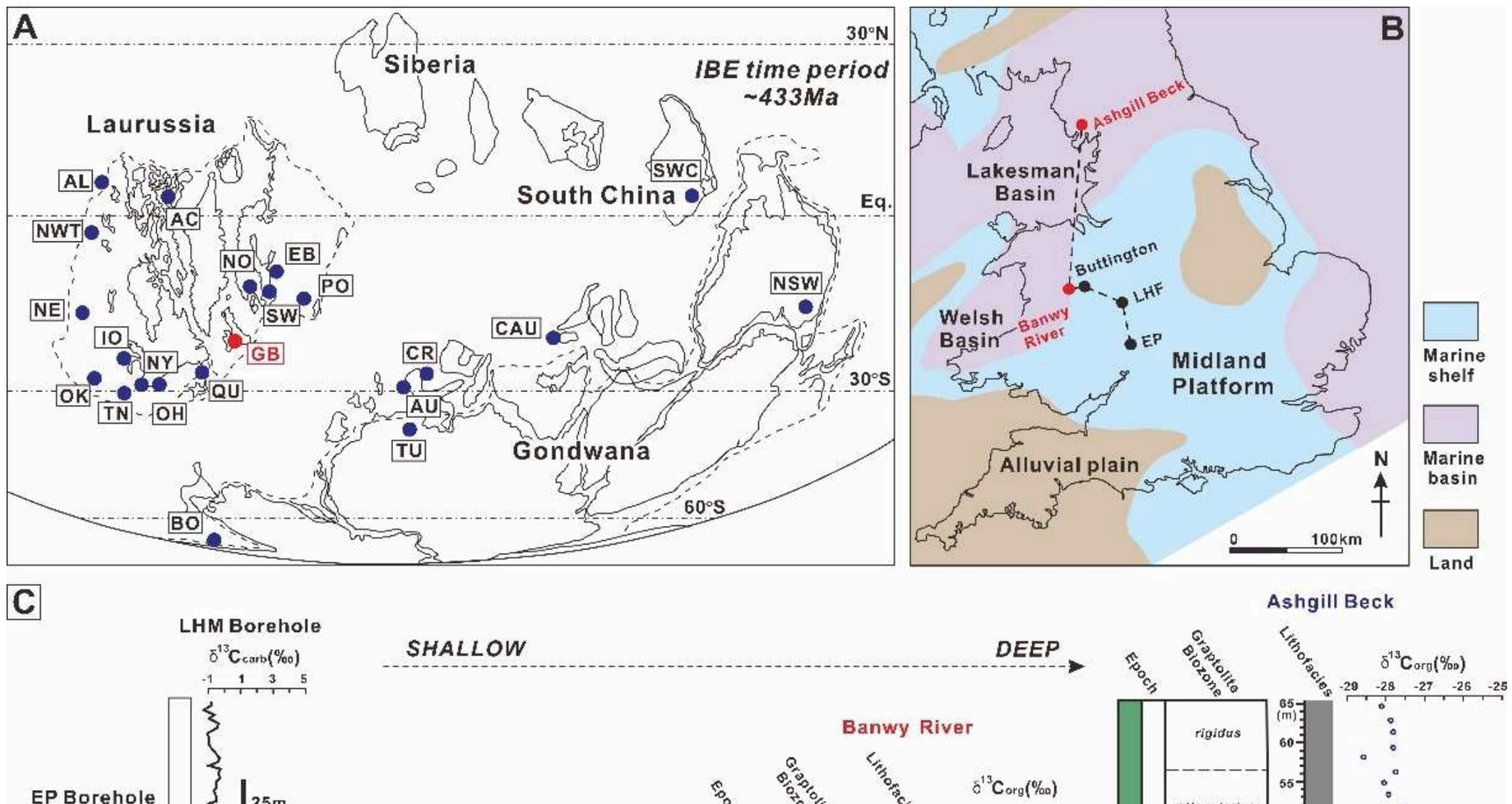

Figure S1: A. Global paleogeography of the late Llandovery, Silurian, showing locations where the Ireviken Extinction Event (IEE) or Early Sheinwoodian Carbon Isotope Excursion (ESCIE) have been documented (after *(1)*). Abbreviations: Alaska (AL), Arctic Canada (AC), Austria (AU), Bolivia (BO), Greater Caucasus region (CAU), Czech Republic (CR), East Baltic (EB), Iowa (IO), Nevada (NE), New South Wales (NSW), New York&Ontario (NY), North West Territories (NWT), Norway (NO), Ohio (OH), Oklahoma (OK), Podolia (PO), Quebec (QU), South West China (SWC), Sweden (SW), Tennessee (TN), Tunisia (TU). Our study area (Great Britain) is highlighted in red. B. Sites where the Ireviken event is recorded in England and Wales, and a paleogeographical map of the depositional environment during the mid-Silurian (modified after British Geological Survey web graph, https://earthwise.bgs.ac.uk). Carbonate platform boreholes (LHF = Lower Hill Farm, EP = Eastnor Park) are from *(15)*. C. Carbon isotope stratigraphy and biozones from the Welsh Basin, Lakesman Basin, and the adjacent Midland Platform. Carbonate carbon isotope ($\delta^{13}C_{carb}$) data for the inner-shelf LHF and EP boreholes are from *(15)*. The $\delta^{13}C_{carb}$ data for the mid-shelf Buttington section are from *(16)*. Organic carbon isotope ($\delta^{13}C_{org}$) data for the outer-shelf Banwy River section and the basin-center Ashgill Beck section are from this study, and the blue dashed line represents the lower resolution data of ref.[15]. Abbreviations: S - start of the ESCIE; *P.a.* - *Pterospathodus amorphognathoides* Biozone; *P.c.* - *Pterospathodus celloni* Biozone; *P.p.* - *Pterospathodus procerus* Biozone *(15)*.

Banwy River Section

The Banwy River section in Wales comprises a continuous, mudstone-dominated succession spanning much of the Llandovery to lower Wenlock interval, from green mudstones in the Telychian *crispus* Biozone to black mudstones in the Sheinwoodian *rigidus* Biozone *(18)* (Fig. S2). Bioturbated layers are present in the grey and medium-grey mudstones of the Telychian and lowermost Sheinwoodian strata, but are absent in the upper Sheinwoodian, which consists solely of finely laminated black mudstones (Fig. S2). Red mudstones occur in the lower section between the *crispus* and *spiralis* graptolite biozones. Thin bentonites occur within the *spiralis* Biozone. We logged the ~190 m section and collected 139 mudstone samples for geochemical analysis (see Tables S1 and S2).

The Banwy River section has a well-constrained graptolite biostratigraphy *(18)* and existing $\delta^{13}C_{carb}$ and $\delta^{13}C_{org}$ records *(23,12)*. Previously sampled at moderate stratigraphic resolution, the $\delta^{13}C_{carb}$ record has previously been utilized *(23)* (Fig. S1C, blue dashed line) to identify the ESCIE onset. Our high-resolution $\delta^{13}C_{org}$ data align closely previous results *(12)*, but provide a more detailed and smoother trend, capturing a maximum $\delta^{13}C_{org}$ increase of ~2‰. Notably, a small negative $\delta^{13}C_{org}$ excursion (~0.7‰) occurs in the *insectus* Biozone, predating the ESCIE (Fig. S1C). This feature corresponds closely with another similar, high-resolution, negative $\delta^{13}C_{org}$ excursion recorded in the Altajme borehole, Gotland, Sweden, immediately before the onset of ESCIE *(24)*. This consistent decoupling of $\delta^{13}C_{org}$ and $\delta^{13}C_{carb}$ in different basins may indicate a perturbation to the global carbon cycle, potentially associated with elevated productivity (*24,25)*. At Banwy

River, the ESCIE terminates in the mid-Sheinwoodian *belophorus* Biozone *(12)*.

Ashgill Beck Section

The Ashgill Beck section, located in the southern Lake District, UK, consists of deep-water mudstone facies that transition from the Browgill Formation of the Stockdale Group to the Brathay Formation of the Tranearth Group *(26)* (Figs. S1, S2). Graptolite biostratigraphy in this section *(19)* begins with the *centrifugus* Biozone and ranges up to the upper Sheinwoodian. We logged 65 m of strata from the uppermost Telychian and into the lower Sheinwoodian, and collected 50 mudstone samples for geochemical analysis (Tables S3 and S4). In this section, a positive $\delta^{13}C_{org}$ excursion occurs, which exceeds 2‰, beginning at the base of the section before declining in the upper *riccartonensis* Biozone.

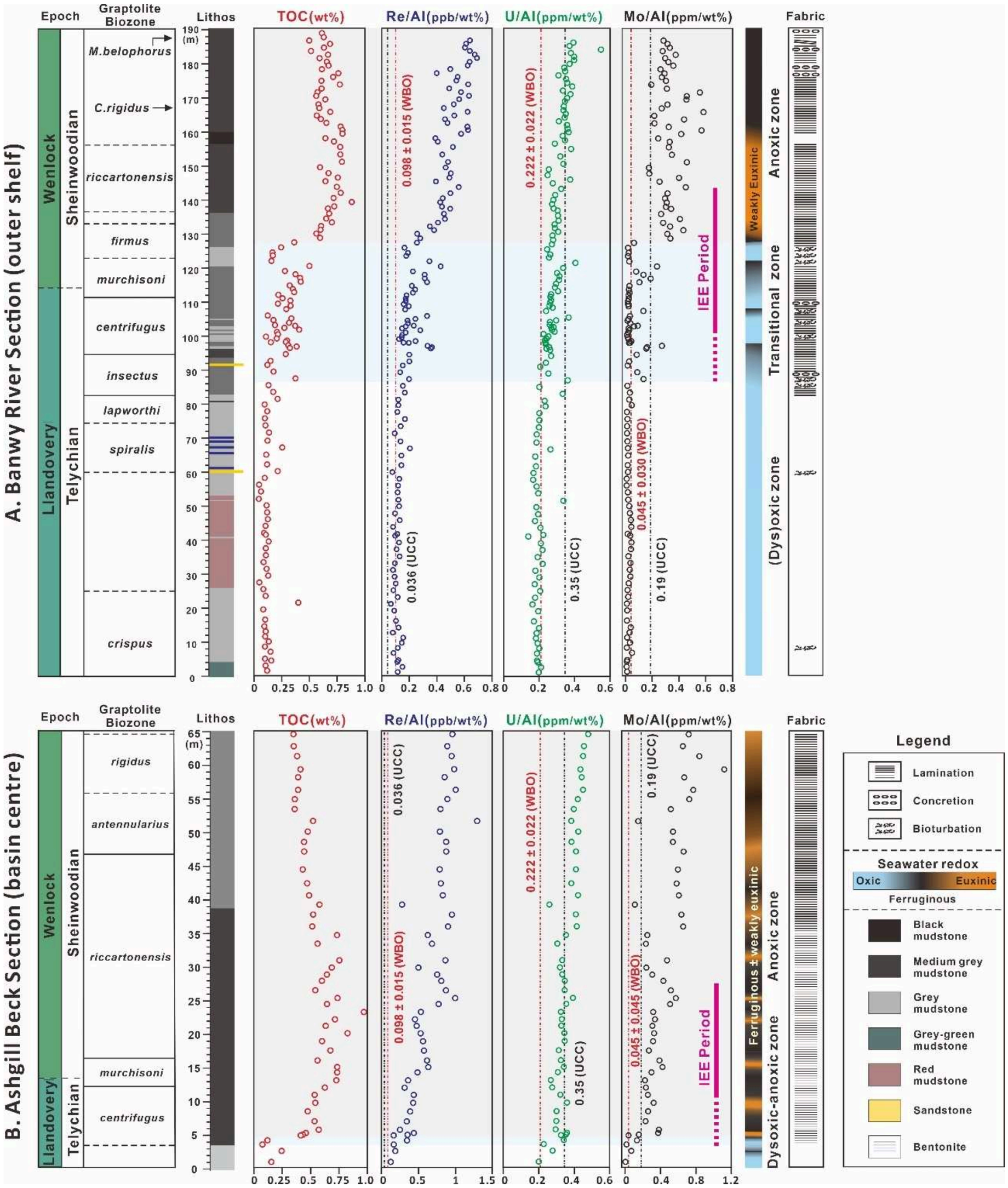

Figure S2: Summary of graptolite biostratigraphy, sedimentological fabrics and geochemical data (TOC, Re/Al, U/Al and Mo/Al) from the deep-shelf Banwy River section (A) and the basinal Ashgill Beck section (B). Graptolite zones are from *(18,19)*. Red dotted lines on the Re/Al, U/Al and Mo/Al plots represent the Welsh Basin oxic baselines (WBO) for the mid-Silurian *(20)*, while the black dotted lines represent average Upper Continental Crust values (Mo and U are from *(21)*; Re is from *(22)*).

Framework for regional redox interpretation

To reconstruct water column redox conditions, we employed independent inorganic redox proxies based on Fe speciation and redox-sensitive trace metal (RSTM) concentrations (see Tables S1 to S4). Iron speciation focuses on the ratio of highly reactive Fe (Fe_{HR}) to total Fe (Fe_T) *(27-29)*. Extensive calibration in both modern and ancient settings (which by definition considers the effects of diagenesis *(30)*) has established general thresholds to differentiate oxic and anoxic depositional conditions *(29,31-37)*. Oxic water column conditions are generally indicated by Fe_{HR}/Fe_T <0.22, while ratios >0.38 suggest anoxic conditions, reflecting additional precipitation of Fe_{HR} phases in the water column *(31)*. Intermediate Fe_{HR}/Fe_T values (0.22-0.38) are considered equivocal and require supplementary evidence to clarify redox conditions *(31)*.

For anoxic samples, the Fe_{py}/Fe_{HR} ratio can be used to distinguish between euxinic and ferruginous conditions. Ratios above 0.6–0.8 typically indicate euxinia *(38-40)*, while ratios <0.6 suggest ferruginous conditions *(31,32)*. Unlike Fe_{HR}/Fe_T ratios, Fe_{py}/Fe_{HR} ratios cannot be calibrated using local oxic samples to establish basin-specific thresholds for anoxic settings *(3)* (see below). Therefore, to support our interpretation of Fe_{py}/Fe_{HR} ratios based on the established thresholds, we incorporate independent evidence from RSTM systematics.

Uranium (U) and molybdenum (Mo) are highly soluble and exhibit limited enrichment in oxic sediments *(41)*. In oxic seawater, U predominantly exists as U(VI) in uranyl carbonate complexes ($UO_2(CO_3)_3^{4-}$) *(42)*, while Mo is stable as Mo(VI) in the molybdate oxyanion (MoO_4^{2-}) *(43)*. Under anoxic conditions at the sediment–water interface, soluble

U(VI) is reduced to insoluble U(IV), primarily at the Fe(II)–Fe(III) redox boundary *(44)*. By contrast, Mo removal requires the presence of elevated concentrations of HS^- in the water column, forming thiomolybdates (MoO_xS_{4-x}) under euxinic conditions *(45,46)*.

Rhenium (Re), by comparison, is enriched just below the sediment–water interface (~1 cm) even under weakly reducing (dysoxic) conditions, where U and Mo enrichment is absent *(47)*. Thus, combined consideration of Re, U and Mo systematics, alongside Fe speciation and Mo/U and Re/Mo ratios, may allow dysoxic, anoxic non-sulphidic (ferruginous) and euxinic conditions to be distinguished at the basin scale *(27)*.

Defining regional oxic baseline values

Recent studies have underscored the importance of calibrating redox interpretations for the specific site of interest, as general redox thresholds are often inappropriate at local or regional scales *(3,28,48-50)*. This is clearly illustrated in the Welsh Basin, where samples from the deepest water section at Borth exhibit Fe_{HR}/Fe_T ratios well below the general oxic baseline value (~0.22; *(31,34)*), while U/Al and Mo/Al ratios are considerably lower than upper continental crust (UCC) values, all supporting oxic depositional conditions *(3)* (Fig. S3). We thus follow a previous approach *(3)* and utilize Borth samples to establish a regional oxic Fe_{HR}/Fe_T range for the Silurian Welsh Basin of 0.081 ± 0.023 (Figs. 2, S3, S4).

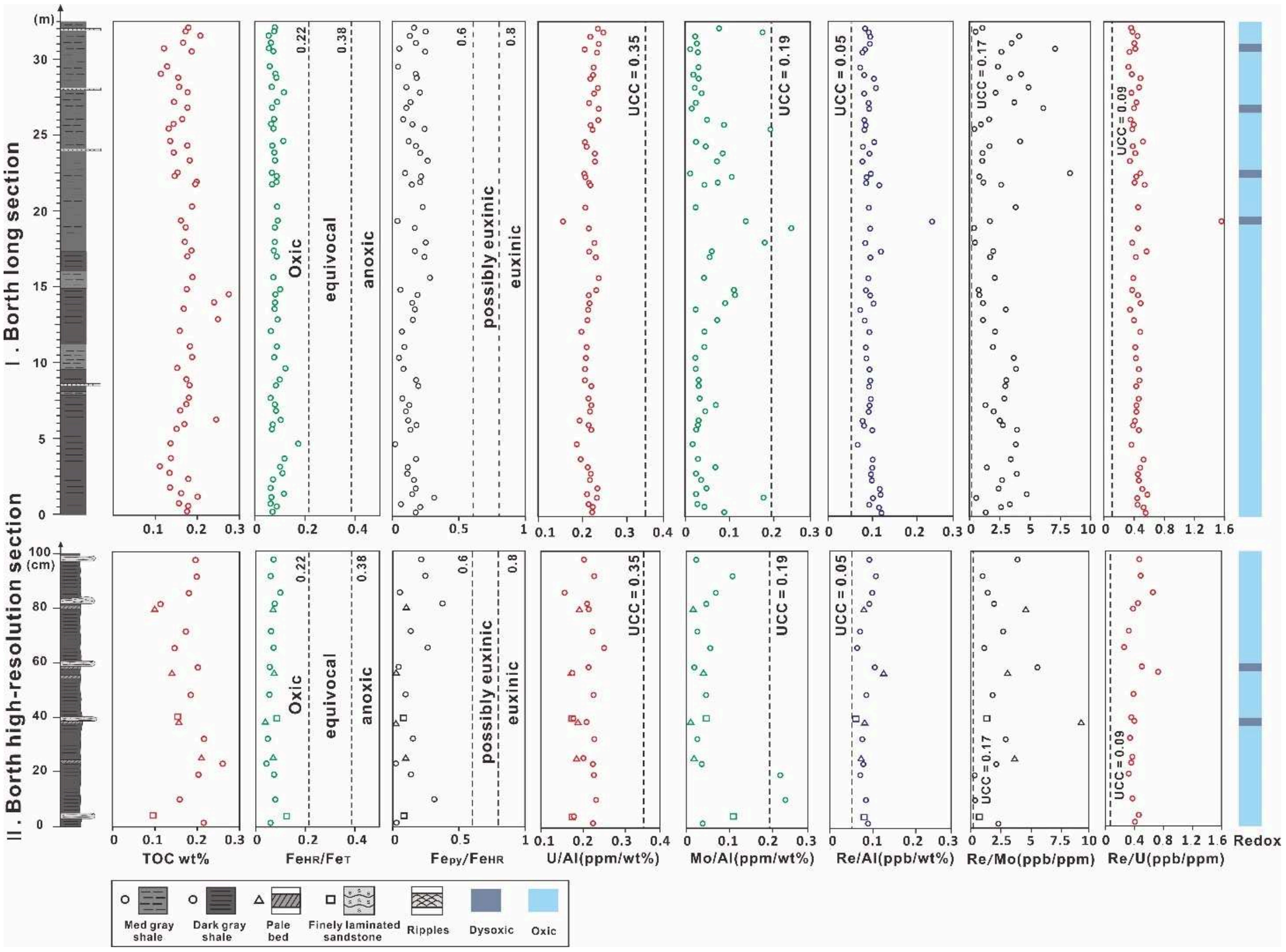

Figure S3: Geochemical data for two Borth sections (data from the *(49)*). For plots involving Re, we calculate ratios relative to the revised crustal average value of 0.29 ppb *(22)*, while crustal averages for Mo, U and Al are from the *(21)*. Possible dysoxic intervals are identified by elevated Re/Mo and/or Re/U ratios *(27)*.

Low U and Mo contents support oxic or dysoxic depositional conditions at the sediment–water interface at Borth *(27,50)*, which we then distinguish utilizing Re systematics. Relatively stable Re/Al ratios that are only slightly above UCC values (~0.036) (Fig. S3), suggest limited drawdown of Re. Furthermore, Re/Mo and Re/U ratios generally fall in the range typical for modern sediments deposited under oxic conditions *(27)* (Fig. S4). These characteristics suggest that, with a few minor exceptions (Fig. S3), the dysoxic conditions required for Re drawdown *(27,47,51)* were largely confined to sediment porewaters during diagenesis. Thus, similar to Fe speciation, we use WBO values *(3)* to define oxic thresholds for Re, U and Mo (Fig. 2). Therefore, non-sulphidic (i.e., ferruginous) water column anoxia is indicated by increased U/Al ratios with low Re/Mo ratios, while euxinia is identified by high Mo/U and very low Re/Mo ratios, alongside high U/Al ratios *(27)*.

Figure S4 shows that there is a high degree of consistency between independent redox proxy data. Specifically, low Fe_{HR}/Fe_T ratios coincide with low U/Al ratios (i.e., where both parameters are lower than the WBO value), supporting (dys)oxic depositional conditions. There is then a general trend of increasing Fe_{HR}/Fe_T and U/Al ratios, suggesting a progressive increase in the intensity or persistence of anoxia *(52, 53)*. Similarly, Mo/Al ratios remain low while Fe_{py}/Fe_{HR} ratios initially increase (Fig. S4), supporting diagenetic sulphide production, where Fe_{HR} phases were progressively sulphidized and Mo drawdown was limited due to the lack of water column euxinia or sulphide generation close to the sediment-water interface. However, as sulphide became more abundant at the sediment-water interface and in the overlying water column, Mo drawdown progressively

increased, giving elevated Mo/Al and Fe_{py}/Fe_{HR} ratios *(52, 53)*.

192

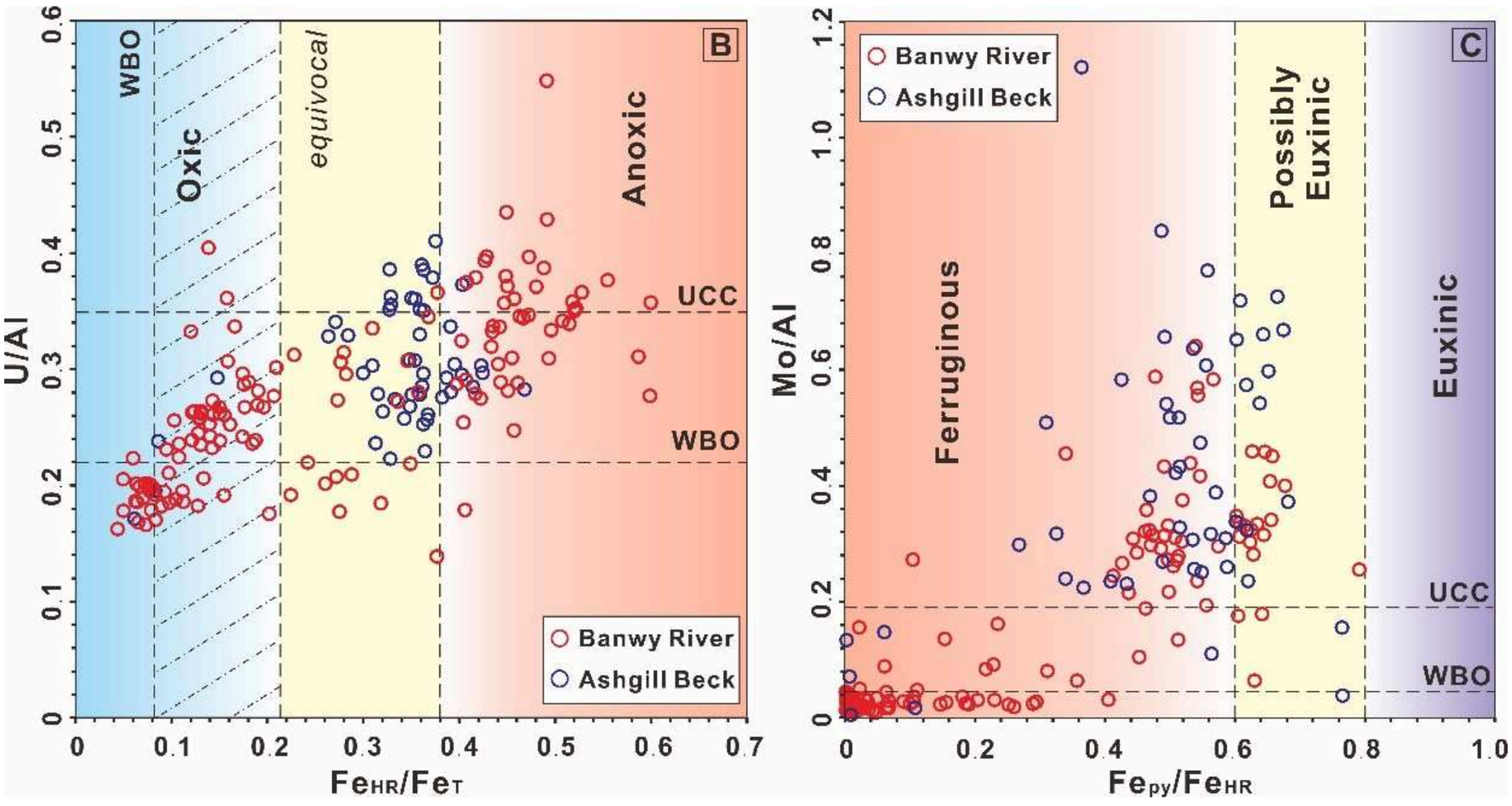

193

194 **Figure S4:** Crossplots showing Fe speciation data, and U/Al and Mo/Al ratios in
195 Telychian-Sheinwoodian sedimentary rocks from the Welsh Basin (Banwy River) and Lakesman
196 Basin (Ashgill Beck). A. U/Al versus Fe_{HR}/Fe_T. The horizontal dashed lines represent the average
197 WBO U/Al value *(3)* and the UCC value *(21)*. B. Mo/Al versus Fe_{Py}/Fe_{HR}. The horizontal dashed lines
198 represent the average WBO Mo/Al value *(3)* and the UCC value *(21)*.

199

Redox zones in the study area

The regional water column redox evolution of the study basins can be delineated into six distinct types (Figs. S5 and S6):

i) Oxic samples from Borth:

These samples, serving as the primary reference for the WBO line, were dominantly deposited under oxic water column conditions and are characterized by low Fe_{HR}/Fe_T and RSTM ratios (Figs. S3, S5, S6).

ii) Red bed samples from the oxic zone of Banwy River:

Collected from 26–53 m height in the section (between the *crispus* and *spiralis* graptolite biozones), these samples exhibit higher Fe_{HR}/Fe_T ratios relative to other oxic-dysoxic samples (Fig. S5). This records an environment with a persistent flux of dissolved Fe^{2+}, which was oxidized in the water column, resulting in sediment enrichment in Fe_{HR} phases, particularly hematite (Fig. 2; Table S1). Redox sensitive trace metal ratios are persistently very low, due to the well-oxygenated conditions both in the water column and during early diagenesis close to the sediment-water interface (Fig. S6).

iii) Samples from the (dys)oxic zone of Banwy River (excluding red bed samples):

These samples have low Fe_{HR}/Fe_T, U/Al and Mo/Al ratios (Fig. 2), suggesting that conditions were not anoxic. However, the occurrence of elevated Re/Al and some high Re/Mo ratios indicates at least the temporal development of dysoxic conditions, promoting Re drawdown *(47,51)* (Figs. 2, S6).

iv) Transitional samples from the Banwy River and Ashgill Beck Sections:

Characterized by somewhat elevated Fe_{HR}/Fe_T and Fe_{py}/Fe_{HR} ratios, and high Re/Al

and U/Al ratios, along with fluctuating Re/Mo values, these samples indicate progressive oxygen depletion relative to the samples noted above, and a water column experiencing fluctuating redox conditions between dysoxic and ferruginous (Figs. 2, S5, S6).

v) Ferruginous anoxic samples from Banwy River and Ashgill Beck:

These samples show markedly elevated Fe_{HR}/Fe_T, Re/Al, U/Al and Mo/Al ratios, accompanied by a substantial decrease in Re/Mo ratios and Fe_{py}/Fe_{HR} values below the threshold of 0.6, indicative of an anoxic ferruginous environment *(55)* (Figs. 2, S5, S6).

vi) Weakly euxinic samples from Banwy River and Ashgill Beck:

These samples exhibit significantly elevated Fe_{HR}/Fe_T, Re/Al, U/Al and Mo/Al ratios. However, they are distinguished by the lowest Re/Mo ratios, with Fe_{py}/Fe_{HR} values that are above the 0.6 threshold but below 0.8, suggesting a weakly euxinic depositional environment (Figs. S5 and S6).

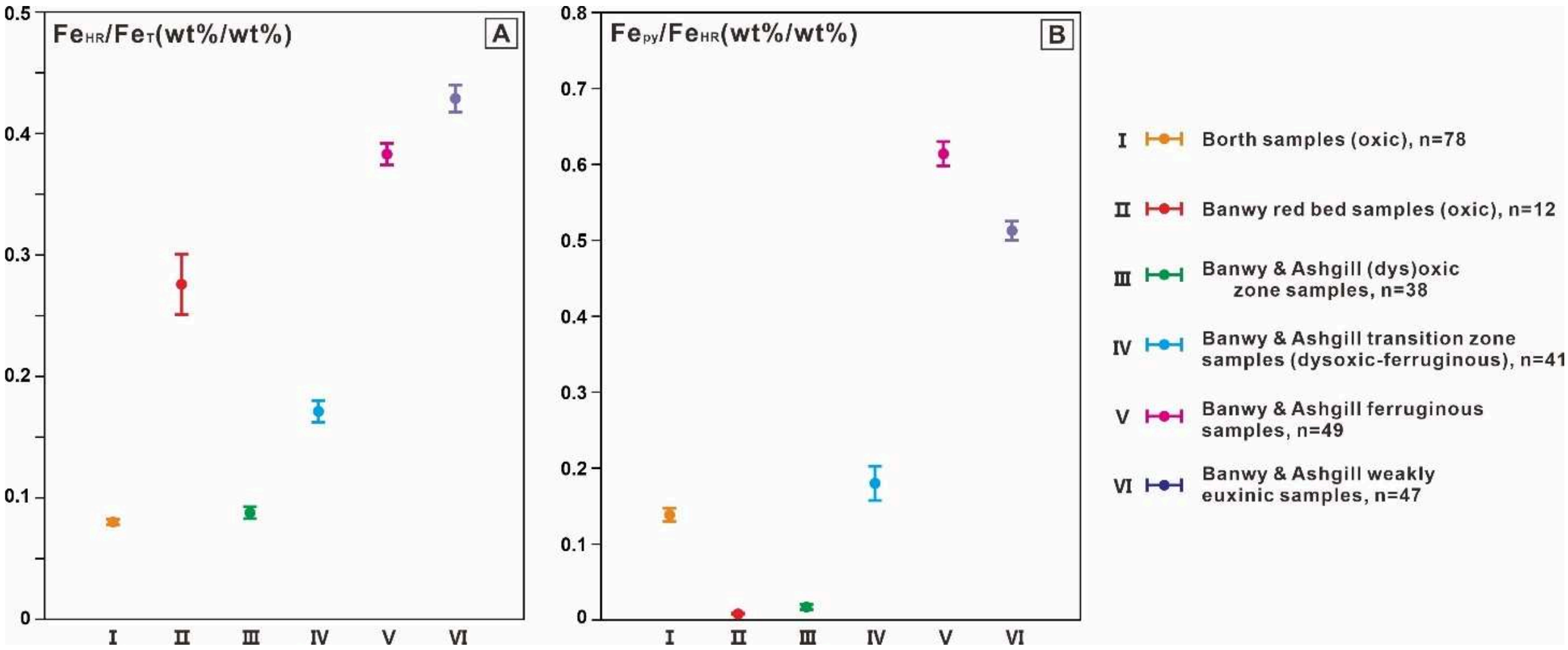

Figure S5: Summary of Fe speciation data for the Borth and Banwy River sections (Welsh Basin) and Ashgill Beck section, Lakesman Basin, UK. Oxic baseline samples are included for the Borth section. Circles represent the mean values, and whiskers represent 1σ.

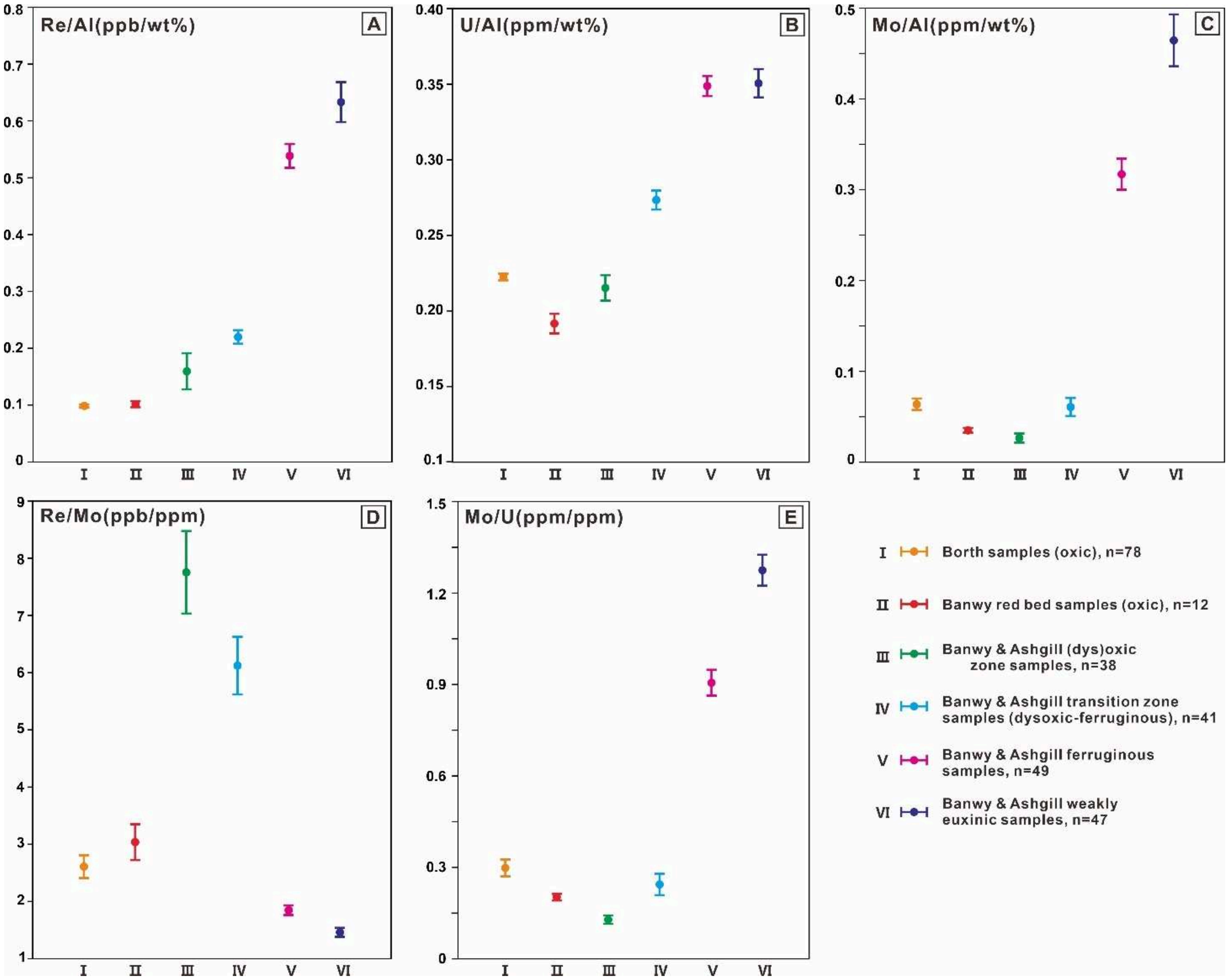

241

242 **Figure S6:** Summary of RSTM data for the Borth, Banwy River and Ashgill Beck sections. Circles
243 represent the mean values and whiskers represent 1σ.

244

Controls on U and Mo Isotope Compositions

Evaluation of detrital influence

To evaluate the potential detrital influence on U and Mo isotope compositions, we first cross-plot U and Mo concentrations against Al, a proxy for terrigenous input (Fig. S7). No significant correlation is observed for samples from Banwy River and Ashgill Beck, with anoxic samples commonly having higher U and Mo contents relative to (dys)oxic samples. This suggests a dominant redox control on U and Mo drawdown into the sediments. Similarly, (dys)oxic samples from both sections tend to exhibit lower U and Mo isotope values compared to samples with ferruginous or weakly euxinic conditions, although there is a degree of overlap in some $\delta^{238}U$ data (Fig. S7). Taken together, these patterns suggest that any detrital influence is negligible for most samples. However, the generally low background concentrations of redox-sensitive elements in our samples precludes the effective application of "excess values" to calculate authigenic U or Mo isotope compositions *(55)*, as this approach results in negative or near-zero "authigenic" values for samples characterized by low U or Mo enrichment. Consequently, we utilize bulk U and Mo isotope values to infer redox conditions.

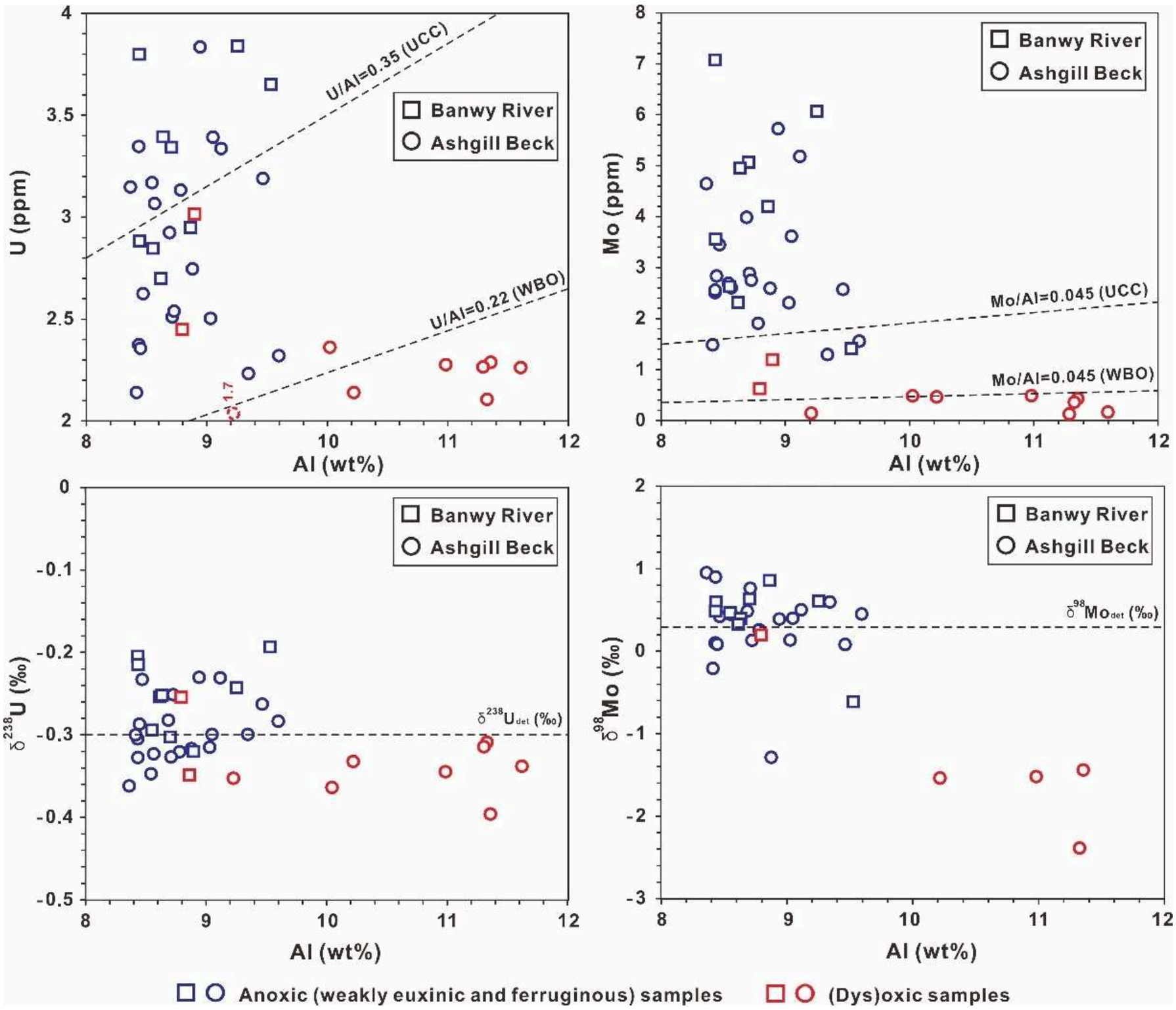

Figure S7: Bulk U and Mo concentrations and isotopic compositions plotted against Al content for samples from Banwy River and Ashgill Beck. The $\delta^{238}U_{det}$ and $\delta^{98}Mo_{det}$ values are estimated using average continental crust values of -0.3‰ and 0.3‰, respectively (*55*, *56*).

Local vs global $\delta^{238}U$-$\delta^{98}Mo$ isotope signatures

Local environmental factors such as organic carbon loading and basin hydrography may influence U isotope fractionations *(57,58)*. In our samples, bulk $\delta^{238}U$ values show no correlation with TOC content (Fig. S8). This may be due to the relatively low TOC content (less than 1 wt%) even in anoxic samples, which could mask the effects of productivity and organic carbon availability on microbial U reduction and isotopic fractionation. Such variability aligns with observations by *(59)*, who reported highly variable $\delta^{238}U$ values in sediments deposited under modern and ancient ferruginous conditions.

Bulk $\delta^{238}U$ values generally covary positively with U/Al, with an increase in both parameters under oxic to anoxic conditions indicating higher authigenic U uptake from seawater under ferruginous or weakly euxinic conditions (Fig. S8). The observed increase in U concentrations and the accompanying shift in $\delta^{238}U$ values from oxic (average −0.33‰) to anoxic samples (average −0.28‰) primarily reflects changes in bottom-water redox conditions. Under increasingly reducing conditions, particularly those that are ferruginous and weakly euxinic, authigenic U uptake becomes more efficient, resulting in both higher U enrichments and more positive $\delta^{238}U$ signatures.

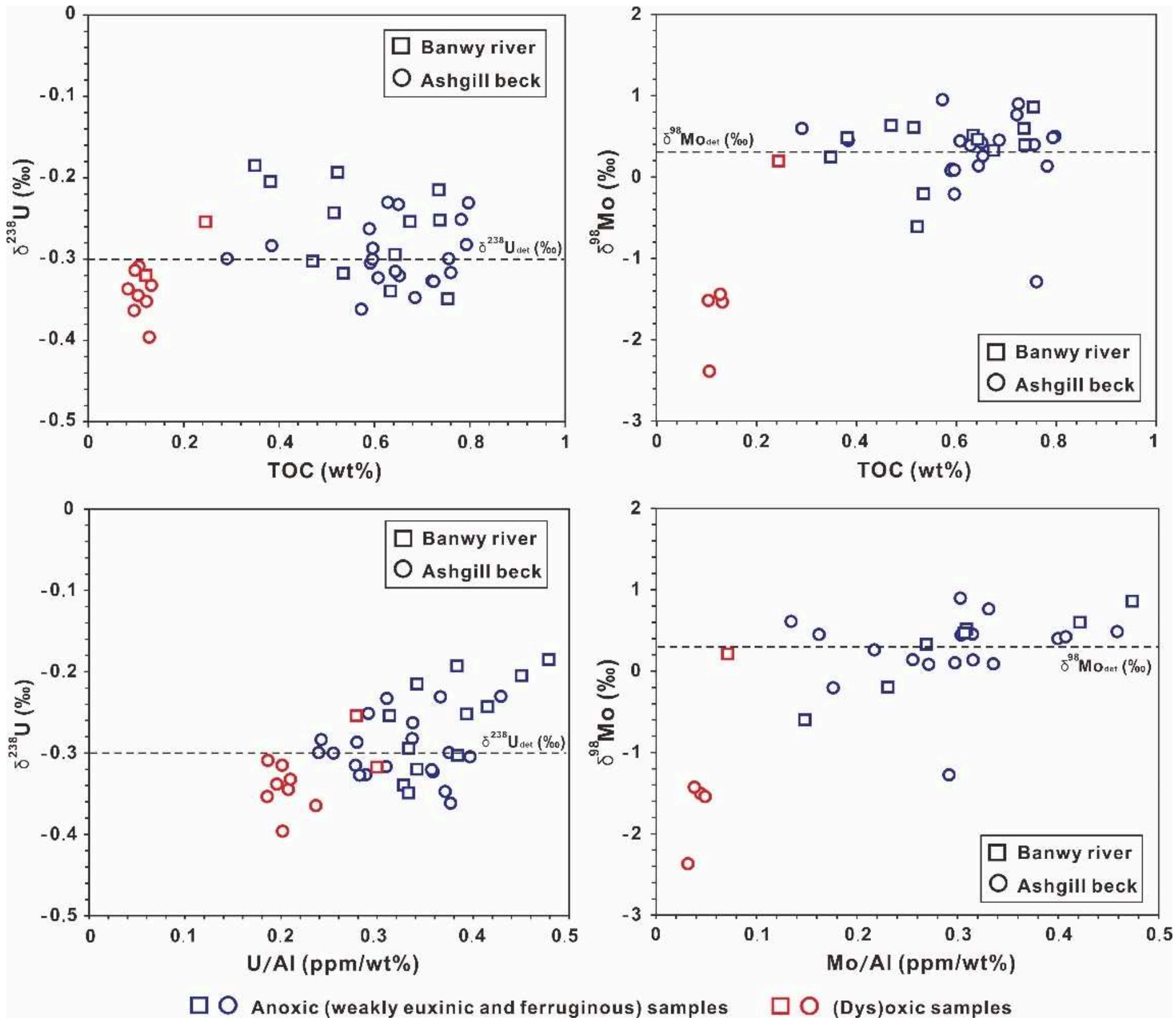

Figure S8: Cross-plots of $\delta^{238}U$ and $\delta^{98}Mo$ versus U and Mo concentrations and total organic carbon (TOC) for samples from the Banwy River and Ashgill Beck sections.

Bulk δ^{98}Mo values show no systematic correlation with TOC or Mo/Al ratios (Fig. S7), suggesting that local organic carbon loading was not the primary control on δ^{98}Mo fractionation *(60)*. In both the Banwy River and Ashgill Beck sections, anoxic samples have higher pyrite contents ($0.6 < Fe_{py}/Fe_{HR} < 0.8$) and elevated Mo/Al ratios (Fig. S3), indicating that enhanced sulfide availability likely drove Mo drawdown into the sediments *(61)*. The data suggest the prevalence of weakly euxinic conditions, which is supported by relatively low Mo/U ratios compared to highly euxinic modern basins (cf. *(27)*), as well as Fe_{py}/Fe_{HR} ratios that generally fall towards the lower end of the 'possibly euxinic' zone (Fig. 2). As a result, Mo was variably and incompletely scavenged from deep waters, leading to highly variable δ^{98}Mo values in ferruginous and weakly euxinic samples (Figs. S7 and S8). The Mo contents of samples for which we have δ^{98}Mo data have an average enrichment of ~7.4 times, increasing from oxic (0.45 ± 0.31 ppm) to anoxic samples (3.32 ± 1.5 ppm) (Table S5). This increase in Mo values from oxic to anoxic samples indicates that, despite incomplete scavenging, a substantial authigenic Mo signal occurs in the anoxic samples. Furthermore, Mo concentrations in oxic red bed samples are likely derived from seawater through adsorption and trapping by Fe-Mn (oxyhydr)oxides, rather than from lithological sources.

Integrating redox constraints from multiple regional proxies (Fe speciation, and Re, U and Mo systematics), particularly when δ^{238}U and δ^{98}Mo are incorporated, provides a robust framework for reconstructing redox conditions from the regional to global scale (Fig. S9; e.g.,*(62-64)*). Collectively, the reductive removal of U and Mo, along with their associated isotopic fractionation, is closely tied to redox evolution and sulphide availability

309 in the water column and/or pore waters. On a broader scale, these processes likely reflect

310 global redox variability during the early to mid-Silurian Period.

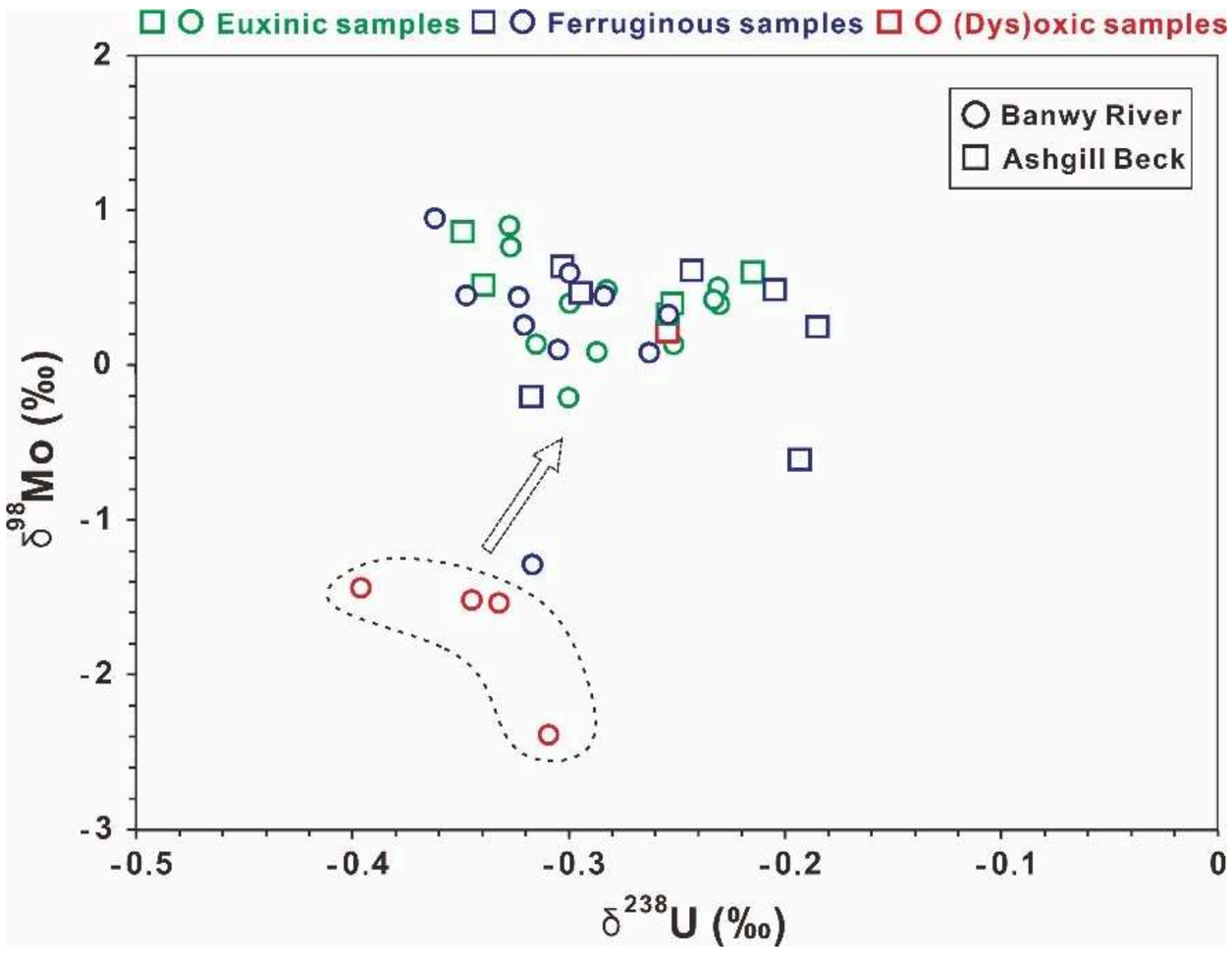

311

312 **Figure S9:** Bulk rock cross-plot of $\delta^{98}Mo$ versus $\delta^{238}U$ for sediments deposited under oxic,
313 ferruginous and weakly euxinic conditions, as determined by Fe speciation and trace metal
314 systematics, in the Banwy River and Ashgill Beck sections. Circled samples (including red bed
315 samples) were collected from the Telychian *crispus* to *spiralis* biozones. The remaining samples
316 were collected from the uppermost Telychian to lower Sheinwoodian (*insectus* to *centrifugus*
317 biozones).

318

Constraining marine redox conditions using the U-Mo isotope system

Reconstruction of seawater $\delta^{98}Mo$ and $\delta^{238}U$

To reconstruct global seawater redox conditions, we combine Mo and U isotope data from the studied rocks, focusing on their well-characterized redox-sensitive behaviour *(55,61)*. Under oxic conditions, Mo is predominantly removed via adsorption onto, or co-precipitation with, Fe–Mn (oxyhydr)oxides, yielding a strong isotopic fractionation (~3‰) between seawater (~ +2.3‰) and modern oxic sediments (~ -0.7‰) *(65-67)*. Based on this, we estimate that the seawater Mo isotope ($\delta^{98}Mo_{SW}$) value during the Telychian red bed interval (the most oxygenated phase in our record), was approximately +1.5‰. By contrast, anoxic samples deposited during the ESCIE interval yield similar $\delta^{98}Mo$ values, consistent with ferruginous to weakly euxinic conditions ($[H_2S]_{aq}$ <11 μM) and incomplete Mo scavenging *(68-70)*. Given that sediments from modern anoxic continental margins typically record $\delta^{98}Mo \approx +0.7‰$ *(71)*, we infer that $\delta^{98}Mo_{SW}$ declined to ~ +1.0‰ during the ESCIE, suggesting a broadening of anoxic seafloor conditions relative to the red bed interval.

Uranium isotopes provide complementary constraints. In oxic seawater, U behaves conservatively, while under reducing conditions it is removed from the water column, with associated isotopic fractionation dependent on the redox state of the depositional environment *(55,72-74)*. Because U is typically enriched in reduced sediments and preferentially incorporates heavier isotopes, authigenic $\delta^{238}U$ values may serve as a maximum estimate for contemporaneous seawater values. For ferruginous and dysoxic samples in this study, we apply a +0.15‰ offset (cf. (*75*)), consistent with sediment $\delta^{238}U$

values between −0.4‰ and −0.2‰ *(59, 76)*. By contrast, the three oxic red bed samples are assigned a −0.23‰ offset, reflecting adsorption of U(VI) onto Fe–Mn (oxyhydr)oxides, which consistently show lower $\delta^{238}U$ relative to seawater *(77, 78)*. Accordingly, we estimate a seawater $\delta^{238}U$ value of ~ −0.13‰ during the red bed interval and ~ −0.49‰ during the ESCIE, consistent with a transition to more widespread marine anoxia.

Combined U-Mo isotope modelling

Sedimentary Mo and U isotope systems are commonly used to evaluate global marine redox conditions in ancient environments through element mass balance and isotope fractionation models (e.g., *(34,79-83)*). However, both local environmental conditions and global ocean redox state may influence the Mo and U isotope compositions of sediments, complicating the interpretation of isotopic data, even in euxinic organic-rich mudstones with significant U and Mo enrichment *(64)*. Stockey *et al.(33)* utilized Monte Carlo simulations and cross-validated LOESS models to estimate potential redox conditions by interpreting U and Mo isotopes separately in euxinic black shales from the Rhuddanian Stage of the lowermost Silurian. By contrast, our study sections lack samples deposited under strong, long-term euxinic conditions, introducing greater uncertainty into the U-Mo isotope system. As discussed above, the $\delta^{98}Mo$ and $\delta^{238}U$ values in our dataset are derived from sediments deposited under oxic, through ferruginous, to weakly euxinic conditions, with low U and Mo concentrations (see Table S6). This results in a much wider range of possible seawater $\delta^{238}U$ and $\delta^{98}Mo$ values, due to variable degrees of fractionation during deposition *(84,71)*.

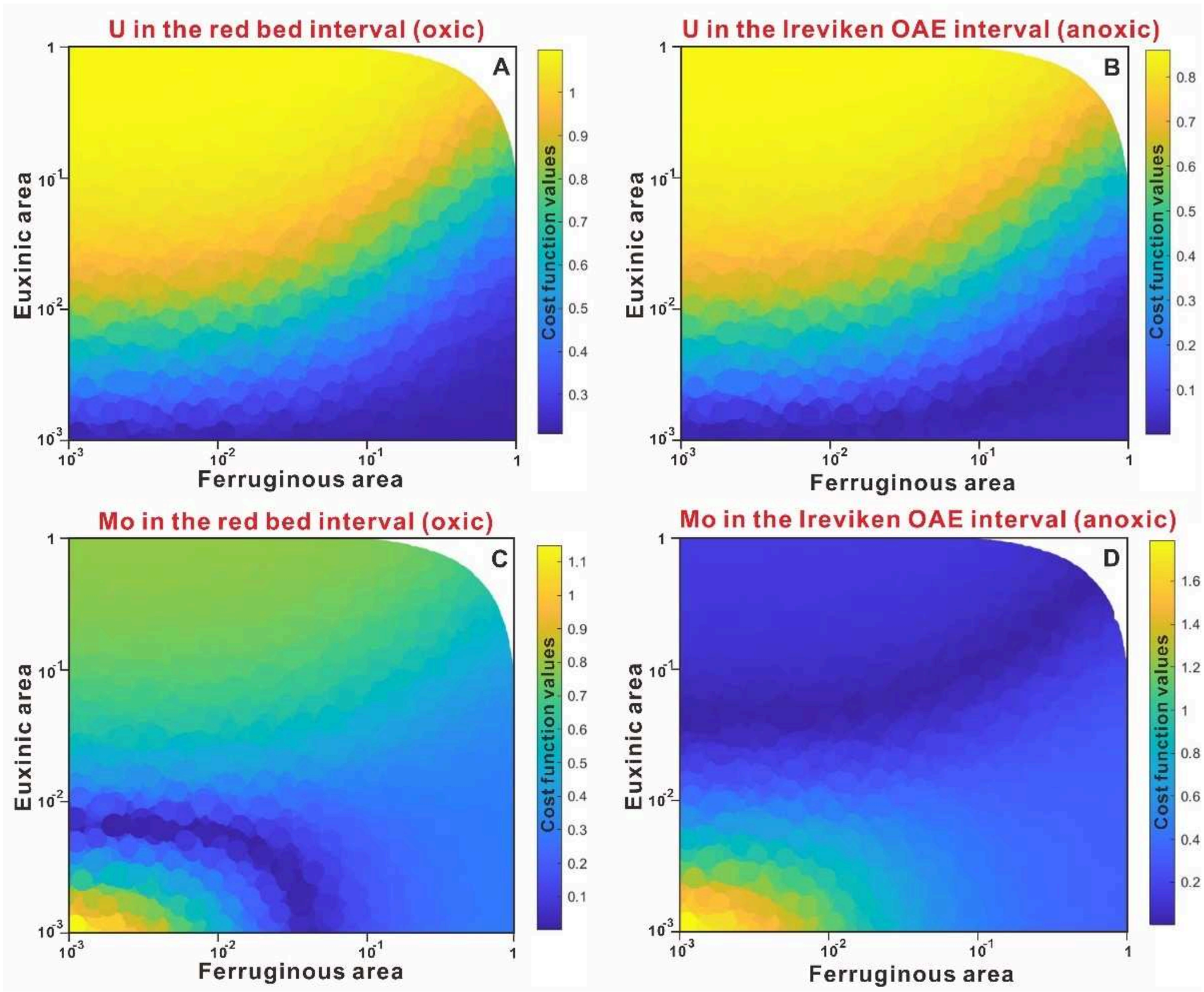

Figure S10: Schematic reconstruction of redox evolution using separate isotope mass balance model outputs for uranium (A and B) and molybdenum (C and D) during the mid Telychian red bed interval and the ESCIE interval. Colored dots represent the mathematical distance (cost function) between 100,000 model iterations and the average laboratory-derived U or Mo isotope fractionation values for the respective intervals. The dark blue shaded regions indicate the lowest cost function values, highlighting the most likely marine redox scenarios.

To address these issues, we ran a large ensemble of isotope mass balance models to determine the marine redox landscape that is most consistent with the combined isotope measurements *(62)*. We used a cost function approach to determine the most likely areal extent of ferruginous and euxinic seafloor. Figure S10 shows the cost function for each isotope measurement considered in isolation, which indicates how close the model isotopic value is to the data for the full range of euxinic and ferruginous seafloor areas tested in the model. For $\delta^{238}U$ (Fig. S10 A, B), ferruginous areas from ~0–100% of the seafloor are all reasonably compatible (i.e., they have a low cost function value), with the data for both oxic mid-Telychian and anoxic ESCIE samples providing limited interpretative value. However, the $\delta^{238}U$ values in our samples certainly do not support widespread marine euxinia (<1%; Fig. S10 A, B), which has a much higher cost function. By contrast, $\delta^{98}Mo$ values show a more pronounced shift between the sampled intervals (Fig. S10 C, D). The average $\delta^{98}Mo$ values change significantly from the mid-Telychian red bed samples (-1.50 ± 0.05‰) to the anoxic IBE samples (0.32‰), reflecting distinct marine redox conditions. In the main text we integrate the $\delta^{98}Mo$ and $\delta^{238}U$ comparisons together within a single cost function framework, in order to determine a more robust redox interpretation for both the Telychian red bed depositional interval and the following ESCIE interval (main text; Fig. 3).

Paleoclimatic controls

Sheinwoodian Oxygen Isotope Excursion (SOIE)

Conodont apatite oxygen isotope ($\delta^{18}O_{phos}$) data from stratigraphic sections in

393 Laurentia (Cornwallis and Anticosti Islands) and Baltica (Estonia and Latvia) reveal a
394 long-term warming trend following the Hirnantian glaciation at the end of the Ordovician.
395 This warming persisted through the Rhuddanian and Aeronian stages until the early-mid
396 Telychian (~437 Ma, *crispus* Biozone). Subsequently, $\delta^{18}O_{phos}$ values indicate a gradual
397 cooling trend beginning in the latest Telychian (*lapworthi* Biozone), culminating in a major
398 early Wenlock cooling peak *(1, 85)*. In detail, the spread of $\delta^{18}O_{phos}$ values in the
399 Llandovery-Wenlock boundary interval suggests an oscillating cooling trend, with an overall
400 increase of 2‰, corresponding to a potential temperature drop of ~9°C (ref. *(85)*). The
401 cooling coincides with evidence for glaciation, including tillites found in the Amazon and
402 Paraná basins of Brazil, as well as the Andean basins of Argentina, Bolivia and Peru, which
403 indicate two phases, the first in the late Telychian and the second in the early
404 Sheinwoodian *(86-88)* (Fig. 4).
405

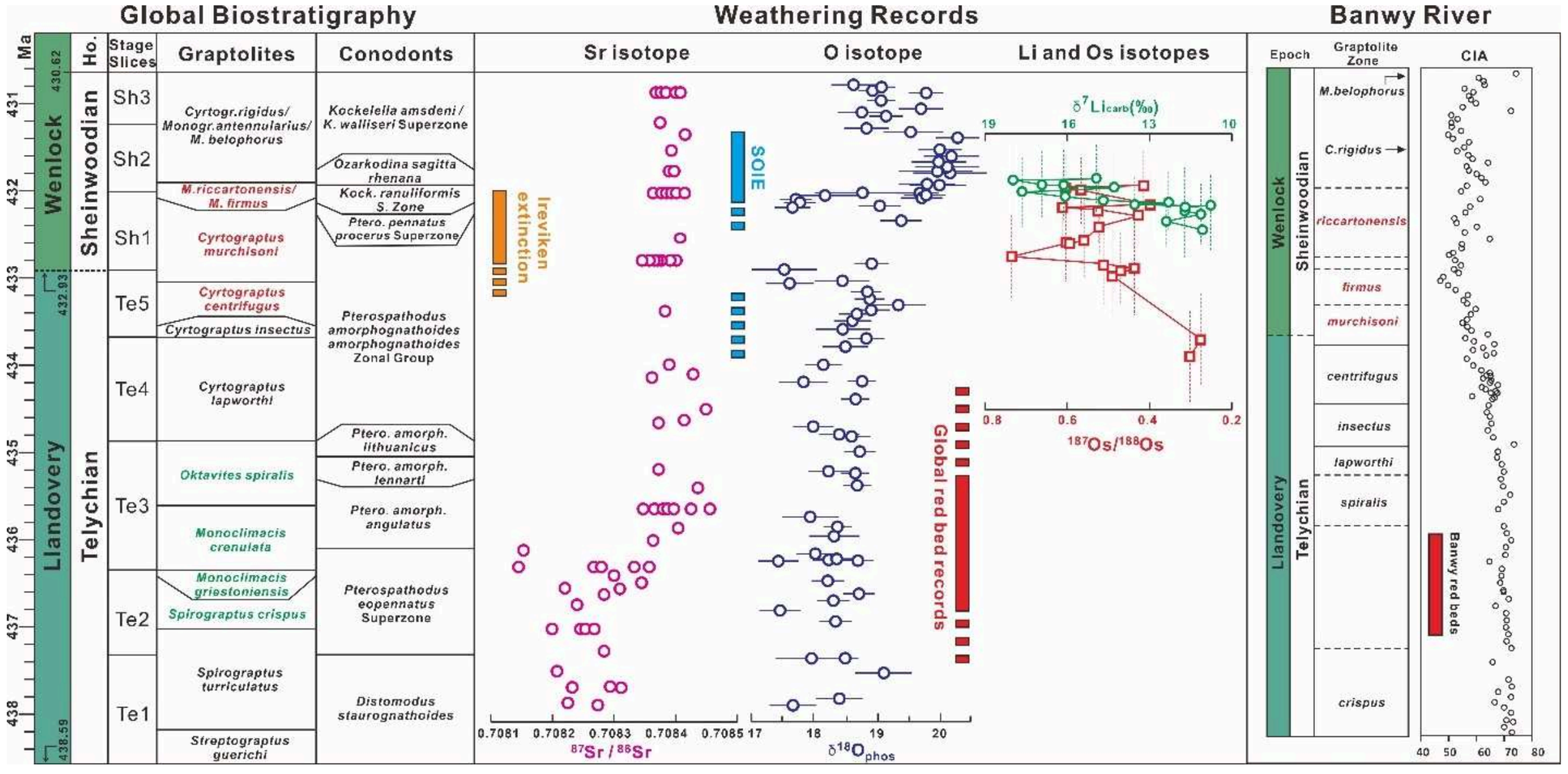

406

407 **Figure S11:** Long term Sr, O, Li and Os isotope records, in the early Silurian *(89)* and the Chemical
408 Index of Alteration (CIA) profile at Banwy River. Data from calcitic brachiopod $^{87}Sr/^{86}Sr$ ratios are
409 from *(90, 91)*. Oxygen isotope records ($\delta^{18}O_{phos}$) of conodont apatite are from *(85)*. Bulk carbonate
410 lithium isotope ($\delta^{7}Li_{carb}$) and shale osmium isotope ($^{187}Os/^{188}Os$) data are from *(92)*.

411

Weathering proxies

A decline in chemical weathering, beginning in the late Telychian, is seen in the chemical index of alteration (CIA) at Banwy River (Fig. S11). The CIA values were calculated as CIA = $Al_2O_3/(Al_2O_3+CaO^*+Na_2O+K_2O) \times 100$, with CaO* representing CaO incorporated into silicate minerals *(93)*. To isolate this component, contributions from carbonate and phosphate minerals were removed following the method of *(94)*. All P_2O_5 was assumed to occur as apatite, and the corresponding CaO was subtracted stoichiometrically. As Ca is more mobile than Na during chemical weathering *(95)*, CaO was taken to equal the remaining CaO if it was less than Na_2O; otherwise, CaO was assumed equivalent to Na_2O. A subtle decline in CIA values occurs as early as the upper part of the *spiralis* Biozone (Fig. S11), potentially documenting a decline in weathering intensity driven by the onset of global cooling *(93,94,96)* considerably before the global expansion of anoxia in the latest Telychian, when CIA values reach a minimum (Fig. 2). This is followed by a degree of variability, with higher CIA values occurring in the late *riccartonensis* Biozone as the water column in the River Banwy section transitioned from weakly euxinic to ferruginous, implying a return to more intense chemical weathering as global climatic conditions recovered during the terminal stage of the ESCIE (Fig. 2).

Calcitic brachiopod shell Sr isotope records from Anticosti Island (Canada), Wales, Gotland (Sweden), Podolia (Ukraine), Latvia and Lithuania reveal progressive increases in $^{87}Sr/^{86}Sr$ values from 0.707930 to 0.708792 through the Silurian, reflecting a possible increased riverine flux of radiogenic Sr to the oceans, driven by enhanced weathering of continental sialic rocks under a progressive, long-term warming climate *(90)*. In the

mid-Telychian, there is an exceptionally rapid increase in $^{87}Sr/^{86}Sr$ values (~0.0003), which may represent a strong silicate weathering peak under warm climatic conditions (Fig. S11). Subsequently, the upward trajectory slows and briefly stabilizes from the mid Telychian to the mid Sheinwoodian, with a slight decrease observed in the lower *murchisoni* Biozone (Fig. S11). While the Silurian long-term $^{87}Sr/^{86}Sr$ trend continues to rise following the end-Ordovician Hirnantian glaciation, this short-term deviation from the broader increase may indicate a temporary decline in silicate weathering rates from the late Telychian into the early Sheinwoodian, potentially linked to early Sheinwoodian cooling and glacial conditions, but given high global sea-level at this time *(18)*, this is unlikely.

The carbonate δ^7Li record from the Lusklint and Lickershamn sections of Gotland exhibits a significant increase in the lower Sheinwoodian, rising from a minimum of 11‰ to a peak of 17.6‰ (Fig. S4; data from *(92)*). Similarly, $^{187}Os/^{188}Os$ isotope ratios in shales and carbonates from the Llandovery to Wenlock interval of the Aizpute-41 core display a general increasing trend, spanning the upper Telychian to lower Sheinwoodian (Fig. S4; data from *(92)*).

The combined evidence of long-term $^{87}Sr/^{86}Sr$ trends through the Telychian and Sheinwoodian stages, with elevated $^{187}Os/^{188}Os$ ratios, and increased δ^7Li and $\delta^{18}O$ values, indicates a change in weathering from a mid-Telychian greenhouse climate to glacial conditions in the early Sheinwoodian. Elevated $^{187}Os/^{188}Os$ ratios and increased δ^7Li values imply enhanced physical erosion coupled with subdued but isotopically distinct chemical weathering. Ice sheet activity may have exposed unweathered bedrock, including radiogenic Os-rich lithologies, such as black shales, which contributed high ^{187}Os fluxes to

the ocean. Simultaneously, freshly-eroded mineral surfaces supported limited chemical alteration under glacial conditions, where fractionation of lithium isotopes occurred as light ^{6}Li was sequestered into secondary clays, leaving heavier ^{7}Li in solution. Enrichment in $\delta^{18}O$ values in phosphate ($\delta\,^{18}O_{phos}$) during the mid-Sheinwoodian (Fig. S11), corroborate the suppression of chemical weathering during cooling *(85)*.

Impact of Ireviken deoxygenation

A comparison of the icehouse-triggered Ireviken deoxygenation event with greenhouse-triggered carbon perturbation events of the Mesozoic demonstrates clear differences (Fig. S12). Unlike Mesozoic OAEs *(99,100)*, the Ireviken deoxygenation appears to have developed in the absence of major volcanism, and instead coincided with global cooling, glacio-eustatic sea-level fluctuations, and the upwelling of ferruginous deep waters under a low-oxygen atmosphere. The well-oxygenated background state of Mesozoic oceans contrasts with that of mid-Paleozoic oceans, which were dysoxic to ferruginous at depth (this study and cf. *(101, 102)*). The longer duration and muted trace metal isotope signatures of Silurian OAEs *(97)* reflect a redox feedback system in which phosphorus recycling was likely suppressed by iron mineral scavenging under ferruginous conditions (e.g., *(103)*), thereby weakening the productivity–anoxia loop that characterized many Mesozoic events (e.g., *(97,104,105)*).

Paleozoic oceanic anoxic events were frequently accompanied by biotic crises, which is a relationship also seen during younger OAEs. The extent of deoxygenation during the Ireviken Event may have approached that of the Permian–Triassic boundary (Fig. S12).

However, the consequences for life were not as severe, an observation that may reflect a somewhat greater resilience of mid-Paleozoic marine life to low oxygen levels when compared to Mesozoic biota.

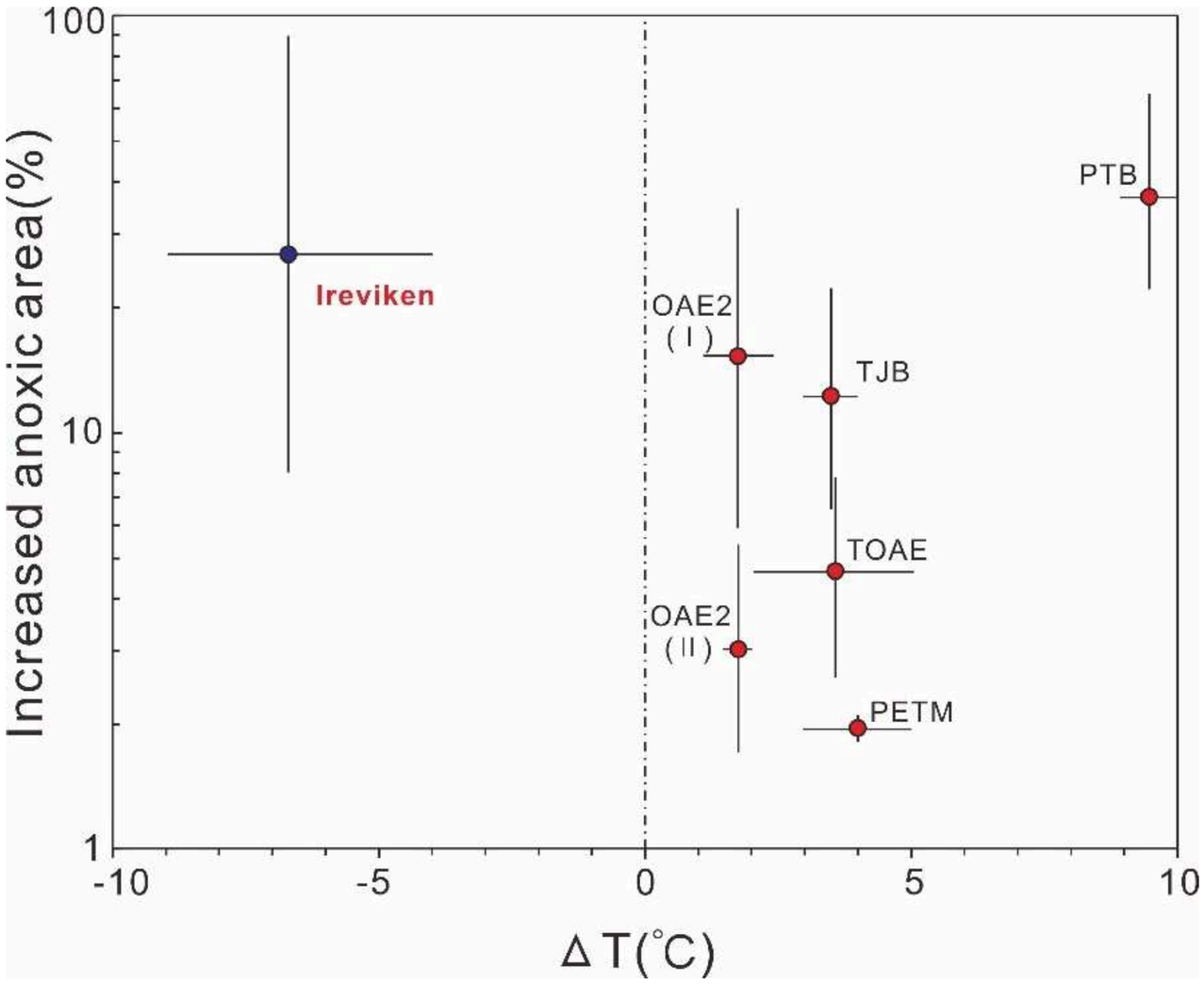

Figure S12: Plot showing the mean increase in marine anoxic area versus temperature change, comparing the cooling-driven Ireviken OAE with warming-driven Mesozoic OAEs. Data are from *(97,98)*. Black lines represent the full range of values used to calculate the mean and are not indicative of error ranges.

References

1 Lehnert O, Männik P, Joachimski M. M., Calner M, Frýda J. Palaeoclimate perturbations before the Sheinwoodian glaciation: A trigger for extinctions during the 'Ireviken Event'. Palaeogeogr. Palaeoclimatol. Palaeoecol. **296**, 320-331 (2010). doi:10.1016/j.palaeo.2010.01.009

2 Jeppsson L. A new latest Telychian, Sheinwoodian and early Homerian (Early Silurian) standard conodont zonation. Trans. R. Soc. Edinb. Earth Sci. **88**, 91-114 (1997). doi:10.1017/S0263593300006854

3 Aldridge R. J., Jeppsson L., Dorning K. J. Early Silurian oceanic episodes and events. J. Geol. Soc. **150**, 501-513 (1993). doi:10.1144/gsjgs.150.3.0501

4 Loydell D. K. Early Silurian positive $\delta^{13}C$ excursions and their relationship to glaciations, sea-level changes and extinction events. Geol. J. **42**, 531-546 (2007). doi:10.1002/gj.1090

5 Cooper R. A., Sadler P. M., Munnecke A., Crampton J. S. Graptoloid evolutionary rates track Ordovician–Silurian global climate change. Geol. Mag. **151**, 349-364 (2014). doi:10.1017/S0016756813000198

6 Calner, M. Silurian global events – at the tipping point of climate change. In Mass Extinction (ed. Elewa, A. M. T.) 21–58 (Springer, Berlin/Heidelberg, 2008). doi:10.1007/978-3-540-75916-4_4

7 Rose C. V., Fischer W. W., Finnegan S., Fike D. A. Records of carbon and sulfur cycling during the Silurian Ireviken Event in Gotland, Sweden. Geochim. Cosmochim. Acta **246**, 299-316 (2019). doi:10.1016/j.gca.2018.12.028

8 Kaljo, D., Martma, T., Neuman, B. E.&Rønning, K. Carbon isotope dating of several uppermost Ordovician and lower Silurian sections in the Oslo Region, Norway. In WOGOGOB-2004: 8th Meeting on the Working Group on the Ordovician Geology of Baltoscandia (Tallinn&Tartu, Estonia, 13–18 May 2004) (Citeseer, 2004).

9 Brand U., Azmy K., Veizer J. Evaluation of the Salinic I tectonic, Cancañiri glacial and Ireviken biotic events: Biochemostratigraphy of the Lower Silurian succession in the Niagara Gorge area, Canada and U.S.A. Palaeogeogr. Palaeoclimatol. Palaeoecol. **241**, 192-213 (2006). doi:10.1016/j.palaeo.2006.04.029

10 Munnecke A., Samtleben C., Bickert T. The Ireviken Event in the lower Silurian of Gotland, Sweden: Relation to similar Palaeozoic and Proterozoic events. Palaeogeogr. Palaeoclimatol. Palaeoecol. **195**, 99-124 (2003). doi:10.1016/S0031-0182(03)00304-3

11 Saltzman M. R. Silurian δ13C stratigraphy: A view from North America. Geology **29**, 671-674 (2001). doi:10.1130/0091-7613(2001)029<0671:SCSAVF>2.0.CO;2

12 Loydell D. K., Frýda J. Carbon isotope stratigraphy of the upper Telychian and lower Sheinwoodian (Llandovery–Wenlock, Silurian) of the Banwy River section, Wales. Geol. Mag. **144**, 1015-1019 (2007). doi:10.1017/S0016756807003895

13 Kaljo D., Martma T. Application of carbon isotope stratigraphy to dating the Baltic Silurian rocks. GFF **128**, 123-129 (2006). doi:10.1080/11035890601282123

14 Cramer B. D., Kleffner M. A., Brett C. E., McLaughlin P. I., Jeppsson L., Munnecke A., Samtleben C. Paleobiogeography, high-resolution stratigraphy, and the future of Paleozoic biostratigraphy: Fine-scale diachroneity of the Wenlock (Silurian) conodont Kockelella walliseri. Palaeogeogr. Palaeoclimatol. Palaeoecol. **294**, 232-241 (2010).

doi:10.1016/j.palaeo.2010.01.00

15 Hughes H. E., Ray D. C. The carbon isotope and sequence stratigraphic record of the Sheinwoodian and lower Homerian stages (Silurian) of the Midland Platform, UK. Palaeogeogr. Palaeoclimatol. Palaeoecol. **445**, 97-114 (2016). doi:10.1016/j.palaeo.2015.12.022

16 Loydell D. K., Frýda J., Butcher A., Loveridge R. F. A new high-resolution $\delta^{13}C_{carb}$ isotope curve through the lower Wenlock Series of Buttington Quarry, Wales. GFF **136**, 172-174 (2014). doi:10.1080/11035897.2013.865668

17 Loydell D. K., Large R. R. Biotic, geochemical and environmental changes through the early Sheinwoodian (Wenlock, Silurian) carbon isotope excursion (ESCIE), Buttington Quarry, Wales. Palaeogeogr. Palaeoclimatol. Palaeoecol. **514**, 305-325 (2019). doi:10.1016/j.palaeo.2018.10.028.

18 Loydell D. K., Cave R. The Llandovery–Wenlock boundary and related stratigraphy in eastern mid-Wales with special reference to the Banwy River section. Newsl. Stratigr. **34**, 39-64 (1996). doi:10.1127/nos/34/1996/39

19 Rickards R. B. Northern England. In A Global Standard for the Silurian System (eds Holland C. H., Bassett M. G.) 116-131 (National Museum of Wales Geological Series 9, Cardiff, 1989).

20 Wang Y., Wignall P. B., Xiong Y., Loydell D. K., Peakall J., Baas J. H., Mills B. J. W., Poulton S. W. Marine redox dynamics and biotic response to the mid-Silurian Ireviken Extinction Event in a mid-shelf setting. J. Geol. Soc. **181**, jgs2023-155, 1-10 (2024). doi:10.1144/jgs2023-155

554 21 McLennan, S. M. Relationships between the trace element composition of sedimentary
555 rocks and upper continental crust. Geochem. Geophys. Geosyst. **2**, 2000GC000109
556 (2001). https://doi.org/10.1029/2000GC000109
557 22 Chen, K., Rudnick, R. L., Gao, S., Walker, R. J., Gaschnig, R. M., Puchtel, I. S., Tang, M. &
558 Hu, Z. Platinum-group element abundances and Re–Os isotopic systematics of the
559 upper continental crust through time: Evidence from glacial diamictites. Geochim.
560 Cosmochim. Acta **191**, 1–16 (2016). https://doi.org/10.1016/j.gca.2016.06.013
561 23 Cramer, B. D., Brett, C. E., Melchin, M. J., Männik, P., Kleffner, M. A., McLaughlin, P. I.,
562 Loydell, D. K., Munnecke, A., Jeppsson, L., Corradini, C., Brunton, F. R.&Saltzman, M. R.
563 Testing the limits of Paleozoic chronostratigraphic correlation via high-resolution
564 (<500 k.y.) integrated conodont, graptolite, and carbon isotope ($\delta^{13}C_{carb}$)
565 biochemostratigraphy across the Llandovery–Wenlock (Silurian) boundary: Is a unified
566 Phanerozoic time scale achievable? Geol. Soc. Am. Bull. **122**, 1700–1716 (2010).
567 https://doi.org/10.1130/B26602.1
568 24 Hartke, E. R., Cramer, B. D., Calner, M., Melchin, M. J., Barnett, B. A., Oborny, S.
569 C.&Bancroft, A. M. Decoupling $\delta^{13}C_{carb}$ and $\delta^{13}C_{org}$ at the onset of the Ireviken Carbon
570 Isotope Excursion: Δ13C and organic carbon burial (forg) during a Silurian oceanic
571 anoxic event. Glob. Planet. Change **196**, 103373 (2021).
572 https://doi.org/10.1016/j.gloplacha.2020.103373.
573 25 Kump, L. R. & Arthur, M. A. Interpreting carbon-isotope excursions: Carbonates and
574 organic matter. Chem. Geol. **161**, 181–198 (1999).
575 https://doi.org/10.1016/S0009-2541(99)00086-4.

576 26 Rickards, R. B. & Woodcock, N. H. Stratigraphical revision of the Windermere
577 Supergroup (Late Ordovician–Silurian) in the southern Howgill Fells, NW England. Proc.
578 Yorks. Geol. Soc. **55**, 263–285 (2005). https://doi.org/10.1144/pygs.55.4.263.
579 27 Li, S., Wignall, P. B. & Poulton, S. W. Co-application of rhenium, vanadium, uranium and
580 molybdenum as paleo-redox proxies: Insight from modern and ancient environments.
581 Chem. Geol. **674**, 122565 (2025). https://doi.org/10.1016/j.chemgeo.2024.122565.
582 28 Poulton, S. W. The Iron Speciation Paleoredox Proxy. (Cambridge Univ. Press, 2021).
583 https://doi.org/10.1017/9781108847148
584 29 Poulton, S. W. & Canfield, D. E. Development of a sequential extraction procedure for
585 iron: Implications for iron partitioning in continentally derived particulates. Chem. Geol.
586 **214**, 209–221 (2005). https://doi.org/10.1016/j.chemgeo.2004.09.003.
587 30 Pasquier, V., Fike, D. A. & Halevy, I. Sedimentary pyrite sulfur isotopes track the local
588 dynamics of the Peruvian oxygen minimum zone. Nat. Commun. **12**, 4403 (2021).
589 https://doi.org/10.1038/s41467-021-24753-x
590 31 Poulton, S. W.&Canfield, D. E. Ferruginous conditions: A dominant feature of the ocean
591 through Earth's history. Elements **7**, 107–112 (2011).
592 https://doi.org/10.2113/gselements.7.2.107.
593 32 Alcott, L. J., Krause, A. J., Hammarlund, E. U., Bjerrum, C. J., Scholz, F., Xiong, Y.,
594 Hobson, A. J., Neve, L., Mills, B. J. W., März, C., Schnetger, B., Bekker, A. & Poulton, S. W.
595 Development of iron speciation reference materials for palaeoredox analysis.
596 Geostand. Geoanal. Res. **44**, 581–591 (2020). https://doi.org/10.1111/ggr.12342.
597 33 Raiswell, R. & Canfield, D. E. Sources of iron for pyrite formation in marine sediments.

Am. J. Sci. **298**, 219–245 (1998). https://doi.org/10.2475/ajs.298.3.219.

34 Poulton, S. W. & Raiswell, R. The low temperature geochemical cycle of iron: From continental fluxes to marine sediment deposition. Am. J. Sci. **302**, 774–805 (2002). https://doi.org/10.2475/ajs.302.9.774.

35 Raiswell, R., Hardisty, D. S., Lyons, T. W., Canfield, D. E., Owens, J. D., Planavsky, N. J., Poulton, S. W. & Reinhard, C. T. The iron paleoredox proxies: A guide to the pitfalls, problems and proper practice. Am. J. Sci. **318**, 491–526 (2018). https://doi.org/10.2475/05.2018.03.

36 Raiswell, R., Newton, R. & Wignall, P. B. An indicator of water-column anoxia: Resolution of biofacies variations in the Kimmeridge Clay (Upper Jurassic, U.K.). J. Sediment. Res. **71**, 286–294 (2001). https://doi.org/10.1306/070300710286.

37 Clarkson, M. O., Poulton, S. W., Guilbaud, R. & Wood, R. A. Assessing the utility of Fe/Al and Fe-speciation to record water-column redox conditions in carbonate-rich sediments. Chem. Geol. **382**, 111–122 (2014). https://doi.org/10.1016/j.chemgeo.2014.05.031.

38 Anderson, T. F. & Raiswell, R. Sources and mechanisms for the enrichment of highly reactive iron in euxinic Black Sea sediments. Am. J. Sci. **304**, 203–233 (2004). https://doi.org/10.2475/ajs.304.3.203.

39 März, C., Poulton, S. W., Beckmann, B., Küster, T., Wagner, T. & Kasten, S. Redox sensitivity of P cycling during marine black shale formation: Dynamics of sulfidic and anoxic, non-sulfidic bottom waters. Geochim. Cosmochim. Acta **72**, 3703–3717 (2008). https://doi.org/10.1016/j.gca.2008.04.025.

40 Benkovitz, A., Matthews, A., Teutsch, N., Poulton, S. W., Bar-Matthews, M. & Almogi-Labin, A. Tracing water-column euxinia in Eastern Mediterranean Sapropels S5 and S7. Chem. Geol. **545**, 119627 (2020). https://doi.org/10.1016/j.chemgeo.2020.119627.

41 Morford, J. L., Martin, W. R., François, R., Carney, C. M., Henson, C. S., Lallier-Vergès, E. A model for uranium, rhenium, and molybdenum diagenesis in marine sediments based on results from coastal locations. *Geochim. Cosmochim. Acta* **73**, 2938–2960 (2009). https://doi.org/10.1016/j.gca.2009.02.029.

42 Calvert, S. E., Pedersen, T. F. Geochemistry of recent oxic and anoxic marine sediments: Implications for the geological record. *Mar. Geol.* **113**, 67–88 (1993). https://doi.org/10.1016/0025-3227(93)90150-T.

43 Zheng, Y., Anderson, R. F., Van Geen, A., Kuwabara, J. S. Authigenic molybdenum formation in marine sediments: A link to pore-water sulfide in the Santa Barbara Basin. *Geochim. Cosmochim. Acta* **64**, 4165–4178 (2000). https://doi.org/10.1016/S0016-7037(00)00495-6.

44 Anderson, R. F., LeHuray, A. P., Fleisher, M. Q., Murray, J. W. Uranium deposition in Saanich Inlet sediments, Vancouver Island. *Geochim. Cosmochim. Acta* **53**, 2205–2213 (1989). https://doi.org/10.1016/0016-7037(89)90347-3.

45 Helz, G. R., Miller, C. V., Charnock, J. M., Mosselmans, J. F. W., Pattrick, R. A. D., Garner, C. D., Vaughan, D. J. Mechanism of molybdenum removal from the sea and its concentration in black shales: EXAFS evidence. *Geochim. Cosmochim. Acta* **60**, 3631–3642 (1996). https://doi.org/10.1016/0016-7037(96)00195-0.

642 46 Zheng, Y., Anderson, R. F., van Geen, A., Fleisher, M. Q. Preservation of particulate
643 non-lithogenic uranium in marine sediments. *Geochim. Cosmochim. Acta* **66**, 3085–
644 3092 (2002). https://doi.org/10.1016/S0016-7037(01)00632-9.
645 47 Crusius, J., Calvert, S., Pedersen, T., Sage, D. Rhenium and molybdenum enrichments in
646 sediments as indicators of oxic, suboxic and sulfidic conditions of deposition. *Earth*
647 *Planet. Sci. Lett.* **145**, 65–78 (1996). https://doi.org/10.1016/S0012-821X(96)00204-X.
648 48 Algeo, T. J., Li, C. Redox classification and calibration of redox thresholds in
649 sedimentary systems. *Geochim. Cosmochim. Acta* **287**, 8–26 (2020).
650 https://doi.org/10.1016/j.gca.2020.01.055.
651 49 Wang, Y., Wignall, P. B., Peakall, J., Baas, J. H., Poulton, S. W. Softgrounds: Substrates
652 controlled by sediment gravity flows and the evolution of deep-water trace fossils.
653 *Geol. Soc. Lond., Spec. Publ.* **556**, SP556-2025-17 (2025).
654 https://doi.org/10.1144/SP556-2025-17.
655 50 Tribovillard, N., Algeo, T. J., Baudin, F., Riboulleau, A. Analysis of marine environmental
656 conditions based on molybdenum–uranium covariation—Applications to Mesozoic
657 paleoceanography. *Chem. Geol.* **324–325**, 46–58 (2012).
658 https://doi.org/10.1016/j.chemgeo.2011.09.009.
659 51 Morford, J. L., Emerson, S. The geochemistry of redox-sensitive trace metals in
660 sediments. *Geochim. Cosmochim. Acta* **63**, 1735–1750 (1999).
661 https://doi.org/10.1016/S0016-7037(99)00126-X.
662 52 He, T., Wignall, P. B., Newton, R. J., Atkinson, J. W., Keeling, J. F. J., Xiong, Y., Poulton, S.
663 W. Extensive marine anoxia in the European epicontinental sea during the end-Triassic

mass extinction. *Glob. Planet. Change* **210**, 103771 (2022). https://doi.org/10.1016/j.gloplacha.2022.103771.

53 Li, S., Wignall, P. B., Xiong, Y., Poulton, S. W., Calibration of redox thresholds in black shale: Insight from a stratified Mississippian basin with warm saline bottom waters. *Geol. Soc. Am. Bull.* **136**, B36915.1 (2024). https://doi.org/10.1130/B36915.1.

54 Matheson, E. J., Pufahl, P. K., Voinot, A., Murphy, J. B., Fitzgerald, D. M. Ironstone as a proxy of Paleozoic ocean oxygenation. *Earth Planet. Sci. Lett.* **594**, 117715 (2022). https://doi.org/10.1016/j.epsl.2022.117715.

55 Andersen, M. B., Stirling, C. H., Weyer, S. Uranium isotope fractionation. *Rev. Mineral. Geochem.* **82**, 799–850 (2017). https://doi.org/10.2138/rmg.2017.82.18.

56 Voegelin, A. R., Pettke, T., Greber, N. D., von Niederhäusern, B., Nägler, T. F. Magma differentiation fractionates Mo isotope ratios: Evidence from the Kos Plateau Tuff (Aegean Arc). *Lithos* **190–191**, 440–448 (2014). https://doi.org/10.1016/j.lithos.2013.12.016.

57 Rutledge, R. L., Gilleaudeau, G. J., Remírez, M. N., Kaufman, A. J., Lyons, T. W., Bates, S., Algeo, T. J. Productivity and organic carbon loading control uranium isotope behavior in ancient reducing settings: Implications for the paleoredox proxy. *Geochim. Cosmochim. Acta* **368**, 197–213 (2024). https://doi.org/10.1016/j.gca.2024.01.007.

58 Lau, K. V., Hancock, L. G., Severmann, S., Kuzminov, A., Cole, D. B., Behl, R. J., Planavsky, N. J., Lyons, T. W. Variable local basin hydrography and productivity control the uranium isotope paleoredox proxy in anoxic black shales. *Geochim. Cosmochim. Acta* **317**, 433–456 (2022). https://doi.org/10.1016/j.gca.2021.10.011.

59 Cole, D. B., Planavsky, N. J., Longley, M., Böning, P., Wilkes, D., Wang, X., Swanner, E. D., Wittkop, C., Loydell, D. K., Busigny, V., Knudsen, A., Sperling, E. A. Uranium isotope fractionation in non-sulfidic anoxic settings and the global uranium isotope mass balance. *Glob. Biogeochem. Cycles* **34**, e2020GB006649 (2020). https://doi.org/10.1029/2020GB006649.

60 Kendall, B., Brennecka, G. A., Wasylenki, L. E., Anbar, A. D., Gordon, G. W., Wang, J., Zheng, W., Romaniello, S. J., Over, D. J., Bennett, Y., Xing, L., Kunert, A., Boyes, C., Liu, J. Inverse correlation between the molybdenum and uranium isotope compositions of Upper Devonian black shales caused by changes in local depositional conditions rather than global ocean redox variations. *Geochim. Cosmochim. Acta* **287**, 141–164 (2020). https://doi.org/10.1016/j.gca.2020.05.008.

61 Kendall, B., Dahl, T. W., Anbar, A. D. The stable isotope geochemistry of molybdenum. *Rev. Mineral. Geochem.* **82**, 683–732 (2017). https://doi.org/10.2138/rmg.2017.82.16.

62 Song, Y., Mills, B. J. W., Bowyer, F. T., Andersen, M. B., Ossa Ossa, F., Dickson, A. J., Harvey, J., Zhang, S., Wang, X., Wang, H., Canfield, D. E., Shields, G. A., Poulton, S. W. Tracking the spatial extent of redox variability in the mid-Proterozoic ocean. *Geology* **53**, 785–789 (2025). https://doi.org/10.1130/G53447.1.

63 Andersen, M. B., Matthews, A., Bar-Matthews, M., Vance, D. Rapid onset of ocean anoxia shown by high U and low Mo isotope compositions of sapropel S1. *Geochem. Perspect. Lett.* **15**, 10–14 (2020). https://doi.org/10.7185/geochemlet.2027.

64 Lu, X., Dahl, T. W., Zheng, W., Wang, S., Kendall, B. Estimating ancient seawater isotope compositions and global ocean redox conditions by coupling the molybdenum and

uranium isotope systems of euxinic organic-rich mudrocks. *Geochim. Cosmochim. Acta* **290**, 76–103 (2020). https://doi.org/10.1016/j.gca.2020.08.032.

65 Barling, J., Arnold, G. L., Anbar, A. D. Natural mass-dependent variations in the isotopic composition of molybdenum. *Earth Planet. Sci. Lett.* **193**, 447–457 (2001). https://doi.org/10.1016/S0012-821X(01)00514-3.

66 Siebert, C., Nägler, T. F., von Blanckenburg, F., Kramers, J. D. Molybdenum isotope records as a potential new proxy for paleoceanography. *Earth Planet. Sci. Lett.* **211**, 159–171 (2003). https://doi.org/10.1016/S0012-821X(03)00189-4.

67 Nakagawa, Y., Takano, S., Firdaus, M. L., Norisuye, K., Hirata, T., Vance, D., Sohrin, Y. The molybdenum isotopic composition of the modern ocean. Geochem. J. 46, 131–141 (2012). https://doi.org/10.2343/geochemj.1.0158.

68 McManus, J., Nägler, T. F., Siebert, C., Wheat, C. G., Hammond, D. E. Oceanic molybdenum isotope fractionation: Diagenesis and hydrothermal ridge-flank alteration. *Geochem. Geophys. Geosyst.* **3**, 1078 (2002). https://doi.org/10.1029/2002GC000356.

69 Poulson, R. L., Siebert, C., McManus, J., Berelson, W. M. Authigenic molybdenum isotope signatures in marine sediments. *Geology* **34**, 617–620 (2006). https://doi.org/10.1130/G22485.1.

70 Siebert, C., McManus, J., Bice, A., Poulson, R., Berelson, W. M. Molybdenum isotope signatures in continental margin marine sediments. *Earth Planet. Sci. Lett.* **241**, 723–733 (2006). https://doi.org/10.1016/j.epsl.2005.11.010.

71 Poulson Brucker, R. L., McManus, J., Severmann, S., Berelson, W. M. Molybdenum behavior during early diagenesis: Insights from Mo isotopes. *Geochem. Geophys. Geosyst.* **10**, Q06010 (2009). https://doi.org/10.1029/2008GC002180.

72 Weyer, S., Anbar, A. D., Gerdes, A., Gordon, G. W., Algeo, T. J., Boyle, E. A. Natural fractionation of $^{238}U/^{235}U$. *Geochim. Cosmochim. Acta* **72**, 345–359 (2008). https://doi.org/10.1016/j.gca.2007.11.012.

73 Holmden, C., Amini, M., François, R. Uranium isotope fractionation in Saanich Inlet: A modern analog study of a paleoredox tracer. *Geochim. Cosmochim. Acta* **153**, 202–215 (2015). https://doi.org/10.1016/j.gca.2014.11.012.

74 Brüske, A., Weyer, S., Zhao, M. Y., Planavsky, N. J., Wegwerth, A., Neubert, N., Dellwig, O., Lau, K. V., Lyons, T. W. Correlated molybdenum and uranium isotope signatures in modern anoxic sediments: Implications for their use as paleo-redox proxy. *Geochim. Cosmochim. Acta* **270**, 449–474 (2020). https://doi.org/10.1016/j.gca.2019.11.031.

75 Wei, G.-Y., Ling, H.-F., Wei, W.-F., Chen, X., Yan, D.-T., Li, D., He, T., Planavsky, N. J., Tarhan, L. G., Wang, D., Shields, G. A., Algeo, T. J. Highly dynamic marine redox state through the Cambrian explosion highlighted by authigenic $\delta^{238}U$ records. *Earth Planet. Sci. Lett.* **544**, 116361 (2020). https://doi.org/10.1016/j.epsl.2020.116361.

76 Andersen, M. B., Vance, D., Morford, J. L., Bura-Nakić, E., Breitenbach, S. F. M., Och, L. Closing in on the marine $^{238}U/^{235}U$ budget. Chem. Geol. 420, 11– 22 (2016). https://doi.org/10.1016/j.chemgeo.2015.10.041.

77 Brennecka, G. A., Wasylenki, L. E., Bargar, J. R., Weyer, S., Anbar, A. D. Uranium isotope fractionation during adsorption to Mn-oxyhydroxides. *Environ. Sci. Technol.* **45**, 1370–1375 (2011). https://doi.org/10.1021/es103061v.

78 Goto, K. T., Anbar, A. D., Gordon, G. W., Romaniello, S. J., Shimoda, G., Takaya, Y., Tokumaru, A., Nozaki, T., Suzuki, K., Machida, S., Hanyu, T., Usui, A. Uranium isotope systematics of ferromanganese crusts in the Pacific Ocean: Implications for the marine $^{238}U/^{235}U$ isotope system. *Geochim. Cosmochim. Acta* **146**, 43–58 (2014).

79 Stockey, R. G., Cole, D. B., Planavsky, N. J., Loydell, D. K., Frýda, J., Sperling, E. A. Persistent global marine euxinia in the early Silurian. *Nat. Commun.* **11**, 1804 (2020). https://doi.org/10.1038/s41467-020-15673-9.

80 Reinhard, C. T., Planavsky, N. J., Robbins, L. J., Partin, C. A., Gill, B. C., Lalonde, S. V., Bekker, A., Konhauser, K. O., Lyons, T. W. Proterozoic ocean redox and biogeochemical stasis. *Proc. Natl Acad. Sci. USA* **110**, 5357–5362 (2013). https://doi.org/10.1073/pnas.1208622110.

81 Dahl, T. W., Hammarlund, E. U., Anbar, A. D., Bond, D. P. G., Gill, B. C., Gordon, G. W., Knoll, A. H., Nielsen, A. T., Schovsbo, N. H., Canfield, D. E. Devonian rise in atmospheric oxygen correlated to the radiations of terrestrial plants and large predatory fish. *Proc. Natl Acad. Sci. USA* **107**, 17911–17915 (2010). https://doi.org/10.1073/pnas.1011287107.

82 Chen, X., Ling, H.-F., Vance, D., Shields-Zhou, G. A., Zhu, M., Poulton, S. W., Och, L. M., Jiang, S.-Y., Li, D., Cremonese, L., Archer, C. Rise to modern levels of ocean oxygenation

769 coincided with the Cambrian radiation of animals. *Nat. Commun.* **6**, 7142 (2015).
770 https://doi.org/10.1038/ncomms8142.

771 83 Clarkson, M. O., Lenton, T. M., Andersen, M. B., Bagard, M.-L., Dickson, A. J., Vance, D.
772 Upper limits on the extent of seafloor anoxia during the PETM from uranium isotopes.
773 *Nat. Commun.* **12**, 399 (2021). https://doi.org/10.1038/s41467-020-20486-5.

774 84 Cole, D. B., Zhang, S., McManus, J. F., Lyons, T. W., Gordon, G. W., Chu, X.-L., Sperling, E.
775 A., Halverson, G. P., McKenzie, N. R., Jiang, G., Cox, G. M., Macdonald, F. A., Planavsky,
776 N. J. Uranium isotope fractionation in non-sulfidic anoxic settings and the global
777 uranium isotope mass balance. *Glob. Biogeochem. Cycles* **34**, e2019GB006331 (2020).
778 https://doi.org/10.1029/2019GB006331.

779 85 Trotter, J. A., Williams, I. S., Barnes, C. R., Männik, P., Simpson, A. New conodont $\delta^{18}O$
780 records of Silurian climate change: Implications for environmental and biological
781 events. *Palaeogeogr. Palaeoclimatol. Palaeoecol.* **443**, 34–48 (2016).
782 https://doi.org/10.1016/j.palaeo.2015.11.011.

783 86 Grahn, Y., Caputo, M. V. Early Silurian glaciations in Brazil. *Palaeogeogr. Palaeoclimatol.*
784 *Palaeoecol.* **99**, 9–15 (1992). https://doi.org/10.1016/0031-0182(92)90003-N.

785 87 Caputo, M. V. Ordovician–Silurian glaciations and global sea-level changes. In *Silurian*
786 *Cycles: Linkages of Dynamic Stratigraphy with Atmospheric, Oceanic and Tectonic*
787 *Changes* (eds Landing, E. & Johnson, M. E.) 15–25 (New York State Museum Bulletin
788 491, 1998).

789 88 Díaz Martínez, E., Grahn, Y. Early Silurian glaciation along the western margin of
790 Gondwana (Peru, Bolivia and northern Argentina): Palaeogeographic and geodynamic

setting. *Palaeogeogr. Palaeoclimatol. Palaeoecol.* **245**, 62–81 (2007). https://doi.org/10.1016/j.palaeo.2006.09.002.

89 Melchin, M. J., Sadler, P. M., Cramer, B. D. The Silurian Period. In *Geologic Time Scale 2020* (eds Gradstein, F. M., Ogg, J. G., Schmitz, M. D. & Ogg, G. M.) 695–732 (Elsevier, 2020). https://doi.org/10.1016/B978-0-12-824360-2.00021-8.

90 Azmy, K., Veizer, J., Wenzel, B., Bassett, M. G., Copper, P. Early Silurian strontium isotope stratigraphy. *Geol. Soc. Am. Bull.* **111**, 475–483 (1999). https://doi.org/10.1130/0016-7606(1999)111<0475:SSIS>2.3.CO;2.

91 Gouldey, J. C., Saltzman, M. R., Young, S. A., Kaljo, D. Strontium and carbon isotope stratigraphy of the Llandovery (Early Silurian): Implications for tectonics and weathering. *Palaeogeogr. Palaeoclimatol. Palaeoecol.* **296**, 264–275 (2010). https://doi.org/10.1016/j.palaeo.2010.05.035.

92 Sproson, A. D., Pogge von Strandmann, P. A. E., Selby, D., Jarochowska, E., Frýda, J., Hladil, J., Loydell, D. K., Slavík, L., Calner, M., Maier, G., Munnecke, A., Lenton, T. M. Osmium and lithium isotope evidence for weathering feedbacks linked to orbitally paced organic carbon burial and Silurian glaciations. *Earth Planet. Sci. Lett.* **577**, 117260 (2022). https://doi.org/10.1016/j.epsl.2021.117260.

93 Nesbitt, H. W., Young, G. M. Early Proterozoic climates and plate motions inferred from major element chemistry of lutites. *Nature* **299**, 715–717 (1982). https://doi.org/10.1038/299715a0.

94 Fedo, C. M., Nesbitt, H. W., Young, G. M. Unraveling the effects of potassium metasomatism in sedimentary rocks and paleosols, with implications for

paleoweathering conditions and provenance. *Geology* **23**, 921–924 (1995). https://doi.org/10.1130/0091-7613(1995)023<0921:UTEOPM>2.3.CO;2.

95 McLennan, S. M. Weathering and global denudation. *J. Geol.* **101**, 295–303 (1993). https://doi.org/10.1086/648221.

96 Sheldon, N. D., Tabor, N. J. Quantitative paleoenvironmental and paleoclimatic reconstruction using paleosols. *Earth-Sci. Rev.* **95**, 1–52 (2009). https://doi.org/10.1016/j.earscirev.2009.03.004.

97 Reershemius, T., Planavsky, N. J. What controls the duration and intensity of ocean anoxic events in the Paleozoic and the Mesozoic? *Earth-Sci. Rev.* **221**, 103787 (2021). https://doi.org/10.1016/j.earscirev.2021.103787.

98 Chen, J., Montañez, I. P., Zhang, S., Isson, T. T., Macarewich, S. I., Liu, X., Zhou, J. Marine anoxia linked to abrupt global warming during Earth's penultimate icehouse. *Proc. Natl Acad. Sci. USA* **119**, e2115231119 (2022). https://doi.org/10.1073/pnas.2115231119.

99 Jenkyns, H. C. Geochemistry of oceanic anoxic events. *Geochem. Geophys. Geosyst.* **11**, Q03004 (2010). https://doi.org/10.1029/2009GC002788.

100 Monteiro, F. M., Pancost, R. D., Ridgwell, A., Donnadieu, Y. Nutrients as the dominant control on the spread of anoxia and euxinia across the Cenomanian–Turonian oceanic anoxic event (OAE2): Model–data comparison. *Paleoceanography* **27**, PA4209 (2012). https://doi.org/10.1029/2012PA002351.

101 Sperling, E. A., Melchin, M. J., Fraser, T., Stockey, R. G., Farrell, U. C., Bhajan, L., Brunoir, T. N., Cole, D. B., Gill, B. C., Lenz, A., Loydell, D. K., Malinowski, J., Miller, A. J., Plaza-Torres, S., Bock, B., Rooney, A. D., Tecklenburg, S. A., Vogel, J. M., Planavsky, N.

J., Strauss, J. V. A long-term record of early to mid-Paleozoic marine redox change. Sci. Adv. **7**, eabf4382 (2021). https://doi.org/10.1126/sciadv.abf4382.

102 Stockey, R. G., Cole, D. B., Farrell, U. C., Agić, H., Boag, T. H., Brocks, J. J., Canfield, D. E., Cheng, M., Crockford, P. W., Cui, H., Dahl, T. W., Del Mouro, L., Dewing, K., Dornbos, S. Q., Emmings, J. F., Gaines, R. R., Gibson, T. M., Gill, B. C., Gilleaudeau, G. J., Goldberg, K., Guilbaud, R., Halverson, G., Hammarlund, E. U., Hantsoo, K., Henderson, M. A., Hodgskiss, M. S. W., Jarrett, A. J. M., Johnston, D. T., Kabanov, P., Kimmig, J., Knoll, A. H., Kunzmann, M., LeRoy, M. A., Li, C., Loydell, D. K., Macdonald, F. A., Magnall, J. M., Mills, N. T., Och, L. M., O'Connell, B., Pagès, A., Peters, S. E., Porter, S. M., Poulton, S. W., Ritzer, S. R., Rooney, A. D., Schoepfer, S., Smith, E. F., Strauss, J. V., Uhlein, G. J., White, T., Wood, R. A., Woltz, C. R., Yurchenko, I., Planavsky, N. J., Sperling, E. A. Sustained increases in atmospheric oxygen and marine productivity in the Neoproterozoic and Palaeozoic eras. Nat. Geosci. **17**, 667–674 (2024). https://doi.org/10.1038/s41561-024-01479-1.

103 Qiu, Z., Zou, C., Mills, B. J. W., Xiong, Y., Tao, H., Lu, Y., Liu, X., Xiao, S., Poulton, S. W. A nutrient control on expanded anoxia and global cooling during the Late Ordovician mass extinction. Commun. Earth Environ. **3**, 34 (2022). https://doi.org/10.1038/s43247-022-00412-x.

104 Poulton, S. W., Henkel, S., März, C., Urquhart, H., Flögel, S., Kasten, S. A continental-weathering control on orbitally driven redox–nutrient cycling during Cretaceous Oceanic Anoxic Event 2. Geology **43**, 963–966 (2015). https://doi.org/10.1130/G36837.1.

105 Schobben, M., Foster, W. J., Sleveland, A. R. N., Zuchuat, V., Svensen, H. H., Bond, D. P. G., Grasby, S. E., Greene, S. E., Hammer, Ø., Jansen, M., Ramezani, J. A nutrient control on marine anoxia during the end-Permian mass extinction. Nat. Geosci. **13**, 640–646 (2020). https://doi.org/10.1038/s41561-020-0616-3.

106 Barnes, C. E., Cochran, J. K. Uranium removal in oceanic sediments and the oceanic U balance. Earth Planet. Sci. Lett. **97**, 94–101 (1990). https://doi.org/10.1016/0012-821X(90)90101-3.

107 Tissot, F. L. H., Dauphas, N. Uranium isotopic compositions of the crust and ocean: Age corrections, U budget and global extent of modern anoxia. Geochim. Cosmochim. Acta **167**, 113–143 (2015). https://doi.org/10.1016/j.gca.2015.06.034.

108 Dunk, R. M., Mills, R. A., Jenkins, W. J. A reevaluation of the oceanic uranium budget for the Holocene. Chem. Geol. **190**, 45–67 (2002). https://doi.org/10.1016/S0009-2541(02)00110-9.

109 Scott, C., Lyons, T. W., Bekker, A., Shen, Y., Poulton, S. W., Chu, X., Anbar, A. D. Tracing the stepwise oxygenation of the Proterozoic ocean. Nature **452**, 456–459 (2008). https://doi.org/10.1038/nature06811.

110 Andersen, M. B., Stirling, C. H., Weyer, S. Uranium isotope fractionation. Rev. Mineral. Geochem. **82**, 799–850 (2017). https://doi.org/10.2138/rmg.2017.82.18.

111 Gilleaudeau, G. J., Romaniello, S. J., Luo, G., Kaufman, A. J., Zhang, F., Klaebe, R. M., Kah, L. C., Azmy, K., Bartley, J. K., Zheng, W., Knoll, A. H. & Anbar, A. D. Uranium isotope evidence for limited euxinia in mid-Proterozoic oceans. Earth Planet. Sci. Lett. 521, 150– 157 (2019). https://doi.org/10.1016/j.epsl.2019.06.012.

112 Wei, G.-Y., Ling, H.-F., Wei, W.-F., Chen, X., Yan, D.-T., Chen, X.-B., Liu, Y., Tang, Y.-Z., Cui, H., Li, D.-J., Lu, D.-B., Wang, X.-Q., Wang, M., Li, C., Wilde, S. A., Zhu, M., Shields, G. A. Global marine redox evolution from the late Neoproterozoic to the early Paleozoic constrained by the integration of Mo and U isotope records. Earth-Sci. Rev. **214**, 103506 (2021). https://doi.org/10.1016/j.earscirev.2020.103506.

Supplementary Tables

Table S1. Organic C and pyrite S isotopes, and Fe speciation contents, in Banwy River samples, east Wales, UK.

Name	Height (m)	Lithofacies Description	$\delta^{13}C_{org}$ (‰)	TOC (wt%)	$\delta^{34}S_{py}$ (‰)	Fe_T (wt%)	Fe_{carb} (wt%)	Fe_{ox} (wt%)	Fe_{mag} (wt%)	Fe_{py} (wt%)	Fe_{HR}/Fe_T	Fe_{py}/Fe_{HR}
BR148	188.59	finely laminated, medium grey mudstone	-27.86	0.61	-17.03	4.59	0.82	0.12	0.14	0.98	0.45	0.48
BR147	187.39	finely laminated, medium grey mudstone	-28.45	0.63	-16.69	4.71	0.82	0.11	0.13	1.25	0.49	0.54
BR146	186.39	finely laminated, medium grey mudstone	-27.19	0.50	-13.82	4.42	0.78	0.11	0.15	0.85	0.43	0.45
BR145	185.39	finely laminated, medium grey mudstone	-27.19	0.69	-14.00	4.31	0.84	0.11	0.14	0.98	0.48	0.47
BR144	184.29	finely laminated, medium grey mudstone	-26.91	0.63	-13.93	4.04	0.77	0.10	0.13	0.99	0.49	0.50
BR143	183.29	finely laminated, medium grey mudstone	-27.52	0.51	-14.77	4.35	0.67	0.09	0.13	0.93	0.42	0.51
BR142	182.19	finely laminated, medium grey mudstone	-27.36	0.67	-15.31	4.57	0.78	0.11	0.15	1.12	0.47	0.52
BR141	181.19	finely laminated, medium grey mudstone	-28.00	0.59	-14.72	4.50	0.76	0.11	0.15	0.91	0.43	0.47
BR140	180.09	finely laminated, medium grey mudstone	-26.97	0.66	-12.94	4.40	0.81	0.11	0.15	0.91	0.45	0.46
BR139	178.99	finely laminated, medium grey mudstone	-27.01	0.67	-12.21	4.53	0.94	0.14	0.15	1.07	0.51	0.46
BR138	177.89	finely laminated, medium grey mudstone	-27.86	0.61	-10.63	4.24	0.76	0.11	0.13	1.01	0.47	0.51
BR137	176.69	finely laminated, medium grey mudstone	-27.22	0.76	-13.14	4.37	0.88	0.10	0.13	1.05	0.49	0.49
BR136	175.59	finely laminated, medium grey mudstone	-28.00	0.71	-13.23	4.49	0.93	0.11	0.13	1.16	0.52	0.50
BR135	174.49	finely laminated, medium grey mudstone	-29.22	0.61	-13.06	4.50	0.88	0.10	0.14	1.21	0.52	0.52
BR134	173.39	finely laminated, medium grey mudstone	-29.08	0.77	-14.71	4.63	0.77	0.11	0.12	1.26	0.49	0.56
BR133	172.19	finely laminated, medium grey mudstone	-27.79	0.61	-12.46	4.40	0.84	0.10	0.14	1.11	0.50	0.51
BR132	171.09	finely laminated, medium grey mudstone	-27.34	0.57	-13.65	4.56	0.91	0.11	0.13	1.37	0.55	0.54
BR131	169.99	finely laminated, medium grey mudstone	-26.74	0.56	-13.92	4.68	0.76	0.10	0.13	1.81	0.60	0.65
BR130	168.99	finely laminated, medium grey mudstone	-26.67	0.64	-13.25	4.56	0.86	0.11	0.14	0.57	0.37	0.34

BR129	167.49	finely laminated, medium grey mudstone	-27.23	0.58	-14.71	4.41	0.90	0.11	0.14	1.12	0.51	0.49
BR128	166.39	finely laminated, dark grey mudstone	-28.31	0.59	-11.53	4.07	0.66	0.09	0.11	0.90	0.44	0.51
BR127	165.29	finely laminated, dark grey mudstone	-27.11	0.69	-13.51	4.71	0.81	0.11	0.14	1.39	0.52	0.57
BR126	164.19	finely laminated, dark grey mudstone	-27.03	0.57	-12.38	4.59	0.90	0.14	0.17	0.94	0.47	0.44
BR125	163.09	finely laminated, dark grey mudstone	-27.34	0.60	-10.72	4.58	1.03	0.10	0.12	1.43	0.59	0.53
BR124	161.99	finely laminated, dark grey mudstone	-27.10	0.65	-12.22	4.22	0.74	0.09	0.11	0.94	0.45	0.50
BR123	160.89	finely laminated, dark grey mudstone	-28.84	0.78	-14.11	4.55	0.85	0.11	0.14	0.97	0.46	0.47
BR122	159.89	finely laminated, dark grey mudstone	-27.34	0.80	-15.10	4.60	0.87	0.11	0.14	1.32	0.53	0.54
BR121	158.79	dark grey mudsotne, some pyritic laminae	-28.12	0.80	-11.98	4.62	0.70	0.09	0.12	1.10	0.43	0.55
BR120	157.49	dark grey mudstone, laminae indistinct	-27.98	0.64	-8.42	4.38	0.92	0.12	0.15	0.84	0.46	0.41
BR110	156.49	finely laminated, dark grey mudstone	-27.93	0.72	/	4.57	0.62	0.10	0.09	1.29	0.46	0.61
BR109	154.89	finely laminated, dark grey mudstone	-28.84	0.78	-14.12	4.60	0.60	0.08	0.09	1.29	0.45	0.62
BR108	152.69	finely laminated, dark grey mudstone	-27.68	0.78	-13.16	4.64	0.62	0.08	0.10	1.21	0.43	0.60
BR107	150.49	finely laminated, dark grey mudstone	-29.03	0.79	-12.22	4.72	0.59	0.09	0.10	1.31	0.44	0.63
BR106	148.84	finely laminated, dark grey mudstone	-28.65	0.60	-13.48	4.55	0.06	0.60	0.06	1.11	0.40	0.60
BR105	147.14	finely laminated, dark grey mudstone	-27.15	0.67	-12.82	4.42	0.57	0.07	0.08	1.30	0.46	0.64
BR104	145.84	finely laminated, dark grey mudstone	-28.51	0.76	-12.93	4.78	0.52	0.04	0.07	1.32	0.41	0.68
BR103	144.74	finely laminated, dark grey mudstone	-27.46	0.64	-12.65	4.54	0.47	0.04	0.07	2.15	0.60	0.79
BR102	143.09	finely laminated, dark grey mudstone	-27.06	0.75	-13.40	4.75	0.42	0.16	0.07	1.26	0.40	0.66
BR101	141.29	finely laminated, dark grey mudstone	-28.52	0.78	-14.25	4.62	0.55	0.05	0.07	1.21	0.41	0.64
BR100	139.79	finely laminated, dark grey mudstone	-27.67	0.72	-12.65	4.64	0.57	0.07	0.07	0.95	0.36	0.57
BR99	138.59	finely laminated, dark grey mudstone	-27.14	0.88	-12.82	4.87	0.62	0.05	0.07	0.59	0.27	0.44
BR98	137.29	finely laminated, dark grey mudstone	-27.35	0.72	-16.19	4.51	0.65	0.04	0.07	1.27	0.45	0.62
BR97	136.69	finely laminated, dark grey mudstone	-26.93	0.67	/	4.65	0.60	0.04	0.07	1.34	0.44	0.66
BR96	135.19	finely laminated, medium grey mudstone	-28.85	0.68	-16.59	4.48	0.56	0.08	0.07	0.53	0.28	0.43
BR95	133.69	finely laminated, medium grey mudstone	-29.10	0.65	-16.80	4.61	0.62	0.04	0.06	1.37	0.45	0.65

BR94	132.59	finely laminated, medium grey mudstone	-27.05	0.70	-17.04	4.45	0.54	0.05	0.07	1.11	0.40	0.63
BR93	131.49	finely laminated, medium grey mudstone	-26.69	0.61	-16.23	4.41	0.59	0.05	0.07	1.24	0.44	0.63
BR92	130.39	finely laminated, medium grey mudstone	-27.05	0.60	-15.86	4.49	0.65	0.07	0.07	0.76	0.35	0.49
BR91	129.29	finely laminated, medium grey mudstone	-27.09	0.56	-17.30	4.64	0.63	0.07	0.07	1.19	0.42	0.61
BR90	127.98	finely laminated, medium grey mudstone	-27.19	0.60	-18.65	4.67	0.64	0.04	0.08	1.18	0.42	0.61
BR89	126.68	finely laminated, medium grey mudstone	-28.35	0.36	-15.73	4.65	0.46	0.04	0.08	0.98	0.34	0.63
BR88	125.18	medium grey mudstone	-27.60	0.24	/	5.17	0.44	0.05	0.15	0.02	0.13	0.02
BR87	123.68	medium grey mudstone	-28.17	0.17	/	5.62	0.47	0.05	0.16	0.01	0.12	0.01
BR86	122.78	medium grey mudstone	-27.77	0.17	-15.80	5.89	0.37	0.05	0.15	0.04	0.10	0.07
BR85	121.18	medium grey mudstone	-27.52	0.16	-23.63	4.02	0.33	0.03	0.15	0.04	0.14	0.07
BR84	119.68	finely laminated, medium grey mudstone	-28.55	0.50	-19.80	4.40	0.49	0.05	0.09	0.74	0.31	0.54
BR83	118.18	finely laminated, medium grey mudstone, small burrows	-27.63	0.28	-20.98	3.88	0.45	0.03	0.08	0.25	0.21	0.31
BR82	117.23	finely laminated, medium grey mudstone	-28.96	0.37	/	4.45	0.47	0.04	0.10	0.64	0.28	0.51
BR81	116.13	finely laminated, medium grey mudstone	-27.22	0.42	-17.57	4.69	0.44	0.04	0.09	0.49	0.23	0.46
BR80	115.03	finely laminated, medium grey mudstone	-27.28	0.42	-16.77	4.52	0.51	0.08	0.10	0.58	0.28	0.45
BR79	113.93	finely laminated, medium grey mudstone	-28.56	0.32	-18.26	4.54	0.48	0.04	0.11	0.19	0.18	0.23
BR78	112.83	finely laminated, medium grey mudstone	-28.04	0.35	-21.46	4.55	0.44	0.04	0.12	0.11	0.16	0.16
BR77	111.93	finely laminated, medium grey mudstone	-28.38	0.36	-17.54	4.84	0.40	0.04	0.13	0.38	0.20	0.41
BR76	111.13	medium grey mudstone with burrows	-28.83	0.22	-13.54	4.92	0.38	0.05	0.14	0.06	0.13	0.10
BR75	110.13	finely laminated, medium grey mudstone	-28.64	0.26	-19.24	5.02	0.43	0.04	0.14	0.14	0.15	0.19
BR74	109.43	finely laminated, medium grey mudstone	-27.43	0.33	/	4.96	0.37	0.04	0.14	0.19	0.15	0.26
BR73	108.53	light grey mudstone with concretions	-27.47	0.22	-20.33	4.98	0.45	0.04	0.14	0.01	0.13	0.02
BR72	107.93	finely laminated, medium grey mudstone	-28.73	0.33	-17.68	4.81	0.53	0.06	0.12	0.29	0.21	0.29
BR71	106.93	finely laminated, medium grey mudstone	-28.36	0.29	-14.56	4.51	0.51	0.04	0.12	0.17	0.19	0.20
BR69	105.03	light grey mudstone	-28.40	0.12	-24.56	2.45	0.79	0.02	0.08	0.03	0.38	0.03

BR68	104.18	finely laminated, medium grey mudstone	-27.60	0.34	-25.18	4.74	0.50	0.04	0.13	0.16	0.17	0.19
BR67	103.68	light grey mudstone	-27.72	0.18	/	5.11	0.43	0.08	0.20	0.03	0.14	0.04
BR66	102.88	finely laminated, medium grey mudstone	-27.76	0.32	-17.82	5.01	0.48	0.07	0.15	0.08	0.16	0.11
BR65	102.18	light grey mudstone	-27.51	0.19	/	4.94	0.54	0.04	0.15	0.21	0.19	0.23
BR64	101.98	finely laminated, medium grey mudstone	-27.58	0.37	-17.10	4.98	0.43	0.04	0.13	0.34	0.19	0.36
BR63	101.38	light grey mudstone	/	0.27	-23.35	5.23	0.43	0.05	0.17	0.11	0.14	0.15
BR62	100.83	finely laminated, medium grey mudstone	-27.58	0.41	-13.42	5.07	0.43	0.04	0.16	0.26	0.18	0.29
BR61	100.13	light grey mudstone	-28.53	0.21	/	5.66	0.35	0.06	0.19	0.02	0.11	0.03
BR60	99.43	light grey mudstone	-27.59	0.22	-22.12	5.22	0.57	0.06	0.17	0.04	0.16	0.04
BR59	98.78	light grey mudstone	-27.56	0.11	-27.14	5.40	0.50	0.04	0.17	0.05	0.14	0.06
BR58	98.23	medium grey, laminated mudstone with small burrows	-27.35	0.21	-17.64	5.23	0.37	0.04	0.15	0.19	0.14	0.25
BR57	97.63	medium grey, laminated mudstone with small burrows	-28.02	0.30	-27.46	4.91	0.41	0.04	0.15	0.04	0.13	0.06
BR56	97.18	medium grey, laminated mudstone	-27.43	0.29	-25.14	5.33	0.33	0.04	0.16	0.12	0.12	0.18
BR55	97.13	medium grey mudstone	-27.63	0.15	-24.11	5.92	0.73	0.05	0.20	0.11	0.18	0.11
BR54	96.23	dark, laminated mudstone	-27.93	0.31	-23.55	5.30	0.40	0.05	0.17	0.07	0.13	0.10
BR53	95.83	dark, laminated mudstone	-27.19	0.38	-23.16	5.13	0.48	0.04	0.17	0.21	0.17	0.24
BR52	95.43	dark, laminated mudstone	-28.25	0.32	-24.85	5.27	0.46	0.05	0.16	0.01	0.13	0.02
BR51	93.63	medium grey, laminated mudstone with small burrows	-27.20	0.29	/	5.48	0.52	0.05	0.19	0.21	0.18	0.22
BR50	91.63	medium grey, laminated mudstone with small burrows	-27.38	0.15	/	5.59	0.52	0.04	0.21	0.08	0.15	0.09
BR49	90.43	medium grey mudstone	-27.38	0.12	/	6.10	0.51	0.04	0.21	0.05	0.13	0.07
BR48	88.43	medium grey mudstone	-27.25	0.18	-29.10	5.17	0.46	0.05	0.18	0.04	0.14	0.06
BR47	86.43	dark grey mudstone	-28.47	0.37	-31.24	4.54	0.40	0.06	0.15	0.11	0.16	0.15

BR46	84.43	medium grey mudstone	-27.43	0.13	/	6.08	0.21	0.03	0.14	0.00	0.06	0.01
BR45	82.43	laminated medium grey mudstone	-28.05	0.17	/	4.46	0.36	0.03	0.13	0.01	0.12	0.02
BR44	80.37	finely laminated black shale	-27.27	0.21	/	4.79	0.24	0.03	0.17	0.02	0.09	0.03
BR43	78.72	light grey mudstone	-27.68	0.10	/	5.02	0.28	0.03	0.17	0.06	0.11	0.11
BR44	76.72	light grey mudstone	-27.01	0.12	/	5.78	0.23	0.03	0.15	0.01	0.07	0.02
BR41	74.62	light grey mudstone	-27.01	0.10	/	6.10	0.21	0.08	0.17	0.01	0.08	0.01
BR40	72.52	light grey mudstone	-28.27	0.10	/	5.74	0.21	0.02	0.15	0.01	0.07	0.02
BR39	70.42	light grey mudstone	-27.26	0.14	/	6.38	0.21	0.03	0.16	0.00	0.06	0.01
BR38	68.03	light grey mudstone	-28.32	0.12	/	5.90	0.37	0.04	0.17	0.01	0.10	0.01
BR37	65.99	finely laminated black shale	-27.30	0.25	/	3.72	0.08	0.27	0.12	0.00	0.12	0.01
BR36	63.86	medium grey mudstone	-27.75	0.11	/	5.31	0.25	0.03	0.13	0.01	0.08	0.01
BR34	61.00	light grey mudstone	-28.83	0.12	/	5.83	0.58	0.03	0.13	0.00	0.13	0.01
BR33	59.00	light grey mudstone	-26.31	0.21	/	5.63	0.23	0.00	0.14	0.01	0.07	0.02
BR32	57.00	light grey mudstone	-28.21	0.10	/	6.17	0.24	0.06	0.15	0.00	0.07	0.01
BR31	55.00	light grey mudstone	-27.23	0.05	/	5.20	0.20	0.04	0.09	0.00	0.06	0.01
BR30	53.00	light grey mudstone	-28.59	0.06	/	4.74	0.07	0.31	0.14	0.00	0.11	0.01
BR29	50.80	light creamy mudstone	-28.23	0.04	-28.78	3.06	0.42	0.04	0.04	0.01	0.17	0.01
BR28	48.90	red mudstone	-26.98	0.11	/	5.66	0.08	1.39	0.32	0.00	0.32	0.00
BR27	46.80	red mudstone	-26.91	0.12	/	5.37	0.09	0.03	0.37	0.01	0.09	0.01
BR26	44.80	red mudstone	-27.30	0.12	/	6.15	0.12	1.28	0.29	0.00	0.28	0.00
BR25	42.80	red mudstone	-27.25	0.10	/	5.68	0.00	1.24	0.30	0.00	0.27	0.00
BR24	40.70	light grey mudstone	-27.26	0.09	/	3.42	0.12	0.04	0.05	0.00	0.06	0.01
BR23	40.20	red mudstone	-27.03	0.11	/	5.64	0.04	1.81	0.27	0.00	0.38	0.00
BR22	38.20	red mudstone	-27.20	0.13	/	5.53	0.09	1.21	0.30	0.00	0.29	0.00
BR21	36.20	red mudstone	-27.32	0.11	/	5.66	0.13	1.49	0.34	0.01	0.35	0.00
BR20	34.10	red mudstone	-27.45	0.11	/	6.25	0.19	0.95	0.26	0.00	0.22	0.00

BR19	32.10	red mudstone	-27.40	0.09	/	5.78	0.01	1.07	0.31	0.01	0.24	0.00
BR18	30.10	red mudstone	-27.29	0.11	/	5.83	0.00	1.99	0.36	0.01	0.41	0.00
BR17	28.10	red mudstone	-27.61	0.13	/	6.10	0.04	1.25	0.30	0.01	0.26	0.00
BR16	26.10	red mudstone	-27.53	0.05	/	5.65	0.09	0.81	0.24	0.01	0.20	0.00
BR15	24.10	light grey mudstone	-27.44	0.08	/	5.33	0.13	0.02	0.11	0.01	0.05	0.02
BR14	22.10	light grey mudstone	-27.44	0.11	/	5.28	0.05	0.09	0.12	0.00	0.05	0.01
BR13	20.10	light grey mudstone	-27.37	0.40	/	6.25	0.01	0.12	0.14	0.00	0.04	0.02
BR12	18.10	light grey mudstone	-27.51	0.08	/	5.46	0.21	0.02	0.18	0.00	0.08	0.01
BR11	15.10	light grey mudstone	-27.45	0.10	/	5.51	0.24	0.03	0.19	0.00	0.08	0.00
BR10	13.10	light grey mudstone	-27.28	0.09	/	5.85	0.24	0.02	0.19	0.00	0.08	0.01
BR9	11.60	light grey mudstone	-27.62	0.11	-25.38	5.38	0.19	0.04	0.37	0.01	0.11	0.01
BR8	10.10	light grey mudstone	-27.87	0.10	/	5.98	0.25	0.04	0.24	0.00	0.09	0.00
BR7	8.60	light grey mudstone	-27.68	0.13	/	4.93	0.45	0.03	0.24	0.04	0.15	0.05
BR6	7.10	light grey mudstone	-27.69	0.10	-25.33	4.59	0.19	0.03	0.13	0.01	0.08	0.02
BR5	5.60	light grey mudstone	-27.77	0.15	/	5.02	0.31	0.03	0.18	0.01	0.10	0.02
BR4	3.50	light grey mudstone	-27.78	0.10	/	6.04	0.18	0.03	0.22	0.00	0.07	0.00
BR3	3.00	light grey mudstone	-27.71	0.16	/	6.17	0.29	0.03	0.19	0.01	0.08	0.01
BR2	1.50	grey-green mudstone	-28.19	0.10	/	5.83	0.27	0.03	0.24	0.03	0.10	0.05
BR1	0.00	grey-green mudstone	-28.40	0.12	/	5.88	0.25	0.05	0.17	0.01	0.08	0.01

Table S2. Major and trace element compositions, and CIA values, for Banwy River samples, east Wales, UK.

Name	Height (m)	Lithofacies Description	Al (wt%)	Ca (wt%)	Na (wt%)	K (wt%)	U (ppm)	Mo (ppm)	Re (ppb)	CIA
BR148	188.59	finely laminated, medium grey mudstone	9.03	1.60	1.12	3.17	3.93	5.31	7.97	60.88
BR147	187.39	finely laminated, medium grey mudstone	8.94	2.15	0.10	3.13	3.84	5.73	8.91	62.67
BR146	186.39	finely laminated, medium grey mudstone	8.96	2.12	0.10	3.12	3.53	2.55	5.73	62.96
BR145	185.39	finely laminated, medium grey mudstone	8.54	2.47	1.04	3.02	3.17	2.69	5.21	55.77
BR144	184.29	finely laminated, medium grey mudstone	8.79	1.88	1.07	3.19	4.82	2.92	5.3	58.93
BR143	183.29	finely laminated, medium grey mudstone	8.71	2.18	1.12	3.06	3.3	2.43	5.56	57.31
BR142	182.19	finely laminated, medium grey mudstone	8.63	2.04	1.12	2.97	3.42	3.24	5.82	58.07
BR141	181.19	finely laminated, medium grey mudstone	8.43	1.91	0.89	2.78	3.35	2.51	5.82	59.87
BR140	180.09	finely laminated, medium grey mudstone	8.65	2.59	1.14	3.05	3.22	2.78	5.51	55.07
BR139	178.99	finely laminated, medium grey mudstone	8.24	3.85	0.84	2.76	2.81	2.95	5.13	72.49
BR138	177.89	finely laminated, medium grey mudstone	8.59	3.54	1.12	2.99	2.98	2.25	4.26	50.96
BR137	176.69	finely laminated, medium grey mudstone	8.88	3.12	1.07	3.16	2.75	2.59	3.52	53.25
BR136	175.59	finely laminated, medium grey mudstone	8.61	3.56	1.10	2.98	3.04	2.34	4.73	51.01
BR135	174.49	finely laminated, medium grey mudstone	8.56	3.51	1.12	2.93	3.07	2.6	4.63	51.1
BR134	173.39	finely laminated, medium grey mudstone	8.99	2.85	1.14	3.17	3.48	1.75	5.62	54.5
BR133	172.19	finely laminated, medium grey mudstone	8.60	3.90	1.03	2.98	2.87	2.67	4.2	49.84
BR132	171.09	finely laminated, medium grey mudstone	8.36	3.55	0.84	2.87	3.15	4.65	4.8	51.53
BR131	169.99	finely laminated, medium grey mudstone	8.76	2.43	0.92	2.94	3.13	4.02	5.54	57.37
BR130	168.99	finely laminated, medium grey mudstone	9.13	2.65	1.09	3.28	3.15	4.16	5.12	55.63
BR129	167.49	finely laminated, medium grey mudstone	8.74	3.13	1.10	3.03	2.96	2.75	4.55	53.06
BR128	166.39	finely laminated, dark grey mudstone	9.46	2.47	1.04	3.45	3.19	2.57	4.25	57.1
BR127	165.29	finely laminated, dark grey mudstone	9.06	2.08	1.11	3.13	3.17	5.28	5.63	58.65

BR126	164.19	finely laminated, dark grey mudstone	8.37	1.07	0.99	2.80	2.88	1.8	4.39	64.26
BR125	163.09	finely laminated, dark grey mudstone	8.61	2.40	0.90	3.18	2.68	3.78	3.94	56.51
BR124	161.99	finely laminated, dark grey mudstone	8.78	2.24	0.98	3.20	3.13	1.91	4.17	57.31
BR123	160.89	finely laminated, dark grey mudstone	8.92	1.80	1.05	3.06	3.22	2.89	5.53	60.11
BR122	159.89	finely laminated, dark grey mudstone	9.12	1.48	1.02	3.30	3.34	5.18	5.7	61.82
BR121	158.79	dark grey mudstone, some pyritic laminae	9.36	1.56	0.77	3.29	3.11	3.9	5.38	63.3
BR120	157.49	dark grey mudstone, laminae indistinct	9.09	2.59	0.92	3.26	3.14	2.23	3.52	56.63
BR110	156.49	finely laminated, dark grey mudstone	8.71	3.07	0.72	3.11	2.51	2.88	3.52	54.51
BR109	154.89	finely laminated, dark grey mudstone	9.09	1.85	0.79	3.11	3.45	2.94	4.68	61.4
BR108	152.69	finely laminated, dark grey mudstone	8.60	2.37	0.84	2.86	2.75	2.99	3.76	57.79
BR107	150.49	finely laminated, dark grey mudstone	8.69	2.71	0.91	2.85	2.93	3.99	4.16	56.08
BR106	148.84	finely laminated, dark grey mudstone	8.42	3.42	0.77	3.04	2.14	1.48	3.89	52.07
BR105	147.14	finely laminated, dark grey mudstone	8.62	3.43	0.78	2.93	2.13	1.54	4.31	52.86
BR104	145.84	finely laminated, dark grey mudstone	9.05	2.05	0.84	3.04	3.39	3.62	4.43	60.2
BR103	144.74	finely laminated, dark grey mudstone	9.03	2.88	0.82	3.08	2.5	2.31	3.53	55.88
BR102	143.09	finely laminated, dark grey mudstone	9.20	1.28	0.86	3.07	2.98	4.15	5.13	64.85
BR101	141.29	finely laminated, dark grey mudstone	8.73	3.01	0.86	2.88	2.54	2.75	4.33	54.85
BR100	139.79	finely laminated, dark grey mudstone	8.82	3.03	0.90	2.96	2.47	2.61	3.89	54.66
BR99	138.59	finely laminated, dark grey mudstone	8.94	3.81	0.89	2.99	2.44	2.76	3.77	51.65
BR98	137.29	finely laminated, dark grey mudstone	8.43	3.96	0.82	2.82	2.37	2.56	3.67	50.18
BR97	136.69	finely laminated, dark grey mudstone	8.53	3.48	0.86	2.82	2.6	2.91	4.23	52.35
BR96	135.19	finely laminated, medium grey mudstone	8.60	3.01	0.91	2.82	2.63	2.3	3.86	54.46
BR95	133.69	finely laminated, medium grey mudstone	8.47	3.54	0.88	2.79	2.62	3.45	3.86	51.92
BR94	132.59	finely laminated, medium grey mudstone	8.72	3.24	0.90	2.86	2.51	2.46	3.54	53.66
BR93	131.49	finely laminated, medium grey mudstone	8.28	4.39	0.86	2.73	2.39	2.77	2.87	48.11
BR92	130.39	finely laminated, medium grey mudstone	7.99	4.52	0.87	2.57	2.46	3.46	3.02	47.04

BR91	129.29	finely laminated, medium grey mudstone	8.64	4.09	0.86	2.94	2.38	2.7	2.2	49.81
BR90	127.98	finely laminated, medium grey mudstone	8.45	3.44	0.83	2.74	2.36	2.84	2.34	52.55
BR89	126.68	finely laminated, medium grey mudstone	8.89	2.62	0.91	2.88	2.42	0.57	2.25	56.93
BR88	125.18	medium grey mudstone	8.94	2.92	1.09	2.70	2.19	0.18	1.45	55.38
BR87	123.68	medium grey mudstone	8.64	2.87	0.88	2.35	2.27	0.21	1.61	56.65
BR86	122.78	medium grey mudstone	8.77	2.37	0.91	2.31	2.24	0.17	1.53	59.75
BR85	121.18	medium grey mudstone	8.83	2.96	0.98	2.75	3.57	0.26	3.03	58.04
BR84	119.68	finely laminated, medium grey mudstone	9.05	2.70	0.94	2.94	3.04	2.14	3.85	56.67
BR83	118.18	finely laminated, medium grey mudstone, small burrows	8.93	3.03	0.91	2.92	2.69	0.72	1.99	55
BR82	117.23	finely laminated, medium grey mudstone	9.10	2.66	1.00	2.95	2.86	1.23	2.81	56.74
BR81	116.13	finely laminated, medium grey mudstone	9.14	2.62	0.81	2.79	2.86	1.72	2.84	58.27
BR80	115.03	finely laminated, medium grey mudstone	9.43	1.62	0.81	2.90	2.79	0.99	3.08	64.17
BR79	113.93	finely laminated, medium grey mudstone	9.24	2.80	1.01	3.08	2.67	0.29	1.99	56.04
BR78	112.83	finely laminated, medium grey mudstone	8.94	2.46	0.81	2.58	2.74	0.24	2.14	59.15
BR77	111.93	finely laminated, medium grey mudstone	9.55	1.24	0.87	2.88	2.55	0.3	2.13	66.48
BR76	111.13	medium grey mudstone with burrows	8.91	1.85	0.88	2.48	2.35	0.21	1.57	62.45
BR75	110.13	finely laminated, medium grey mudstone	9.04	2.55	0.86	2.57	2.42	0.22	1.55	58.81
BR74	109.43	finely laminated, medium grey mudstone	9.89	1.33	0.88	2.95	2.59	0.18	1.69	66.35
BR73	108.53	light grey mudstone with concretions	9.11	1.73	0.84	2.59	2.35	0.18	1.43	63.6
BR72	107.93	finely laminated, medium grey mudstone	8.95	2.91	0.79	2.73	2.48	0.22	1.73	56.61
BR71	106.93	finely laminated, medium grey mudstone	9.34	2.14	0.77	2.96	2.23	1.29	1.55	61
BR69	105.03	light grey mudstone	3.73	5.15	/	1.02	1.36	0.13	1.22	/
BR68	104.18	finely laminated, medium grey mudstone	9.18	1.96	0.79	2.83	2.72	0.22	2.22	61.83
BR67	103.68	light grey mudstone	9.00	1.60	0.81	2.65	2.35	0.14	1.65	64.88
BR66	102.88	finely laminated, medium grey mudstone	9.18	1.62	0.88	2.77	2.39	0.34	1.72	63.62
BR65	102.18	light grey mudstone	9.67	1.40	0.87	3.03	2.72	0.89	2.22	65.17

BR64	101.98	finely laminated, medium grey mudstone	9.29	1.80	0.89	2.85	2.5	0.6	1.59	62.49
BR63	101.38	light grey mudstone	9.60	1.42	0.88	2.91	2.62	0.22	1.38	65.39
BR62	100.83	finely laminated, medium grey mudstone	9.52	1.21	1.03	3.09	2.73	0.26	2.64	64.98
BR61	100.13	light grey mudstone	9.67	0.98	1.02	2.87	2.17	0.2	1.65	67.75
BR60	99.43	light grey mudstone	9.29	1.91	0.84	2.90	2.35	0.12	1.35	61.98
BR59	98.78	light grey mudstone	9.29	1.71	0.85	2.84	2.25	0.16	1.31	63.35
BR58	98.23	medium grey, laminated mudstone with small burrows	9.77	1.11	0.88	3.11	2.27	0.22	1.19	66.91
BR57	97.63	medium grey, laminated mudstone with small burrows	9.36	1.29	0.96	2.88	2.2	0.42	2.27	65.27
BR56	97.18	medium grey, laminated mudstone	9.92	1.01	0.94	3.11	2.37	0.36	1.53	67.59
BR55	97.13	medium grey mudstone	8.83	2.65	0.72	2.64	2.08	0.25	1.71	58.52
BR54	96.23	dark, laminated mudstone	9.74	1.21	0.82	3.11	2.51	2.66	3.21	66.56
BR53	95.83	dark, laminated mudstone	9.60	1.28	0.85	3.03	2.32	1.55	3.48	65.79
BR52	95.43	dark, laminated mudstone	9.46	1.39	0.92	3.06	2.48	1.47	3.35	64.42
BR51	93.63	medium grey, laminated mudstone with small burrows	9.57	1.68	0.82	2.99	2.56	0.81	1.88	63.82
BR50	91.63	medium grey, laminated mudstone with small burrows	9.08	1.45	0.86	2.70	2.16	0.26	1.79	64.9
BR49	90.43	medium grey mudstone	9.48	1.53	0.79	2.81	1.95	0.16	1.41	65.46
BR48	88.43	medium grey mudstone	9.70	1.42	1.11	2.99	2.45	0.86	1.27	64.18
BR47	86.43	dark grey mudstone	9.79	1.19	0.89	3.19	3.54	1.33	1.9	66.12
BR46	84.43	medium grey mudstone	10.03	0.75	0.99	3.09	2.02	0.16	1.5	73.62
BR45	82.43	laminated medium grey mudstone	9.80	0.93	0.94	3.12	3.26	0.33	1.61	67.81
BR44	80.37	finely laminated black shale	9.99	0.66	1.04	3.05	2.31	0.29	1.17	67.48
BR43	78.72	light grey mudstone	10.03	0.27	0.73	3.57	2.37	0.48	1.17	69.16
BR44	76.72	light grey mudstone	9.95	0.69	0.87	2.89	2.01	0.12	1.09	69.95
BR41	74.62	light grey mudstone	10.04	0.36	0.90	3.12	2.02	0.15	1.66	68.89
BR40	72.52	light grey mudstone	10.62	0.25	0.85	3.39	2.11	0.14	1.43	69.67
BR39	70.42	light grey mudstone	10.17	0.52	0.73	2.83	1.9	0.12	0.92	72.21

BR38	68.03	light grey mudstone	9.21	0.83	0.83	2.55	1.71	0.14	1.22	69.95
BR37	65.99	finely laminated black shale	10.63	0.20	0.96	3.59	2.8	0.2	2.14	67.86
BR36	63.86	medium grey mudstone	9.55	0.61	1.00	2.72	1.71	0.19	1.32	68.16
BR34	61.00	light grey mudstone	9.80	0.74	0.82	2.95	1.79	0.16	1.36	69.95
BR33	59.00	light grey mudstone	10.22	0.48	0.76	3.08	1.72	0.2	0.75	70.99
BR32	57.00	light grey mudstone	10.49	0.40	0.69	3.03	1.74	0.11	1.3	72.57
BR31	55.00	light grey mudstone	10.65	0.48	0.82	3.23	1.98	0.11	1.23	70.67
BR30	53.00	light grey mudstone	12.02	0.19	0.81	4.03	2.34	0.21	1.34	70.52
BR29	50.80	light creamy mudstone	10.53	1.45	0.84	3.76	3.55	0.22	1.24	64.73
BR28	48.90	red mudstone	10.80	0.39	0.79	3.81	1.99	0.32	1.32	69.23
BR27	46.80	red mudstone	10.45	0.43	0.77	3.72	2.03	0.36	0.97	69.05
BR26	44.80	red mudstone	11.20	0.20	1.03	3.48	1.99	0.46	1.43	68.63
BR25	42.80	red mudstone	10.98	0.46	0.79	3.74	2.28	0.49	0.86	69.77
BR24	40.70	light grey mudstone	10.39	0.24	0.85	3.20	2.32	0.18	1.13	69.85
BR23	40.20	red mudstone	12.13	0.21	0.66	4.18	1.69	0.43	1.15	71.71
BR22	38.20	red mudstone	10.22	0.28	0.98	3.54	2.14	0.46	1.25	66.97
BR21	36.20	red mudstone	10.87	0.18	0.71	3.63	2.38	0.45	1.14	70.77
BR20	34.10	red mudstone	12.33	0.25	0.83	3.99	2.36	0.27	1.56	70.99
BR19	32.10	red mudstone	11.04	0.31	0.70	3.79	2.42	0.43	1.01	70.72
BR18	30.10	red mudstone	11.07	0.20	0.64	3.75	1.98	0.36	0.86	71.56
BR17	28.10	red mudstone	11.36	0.21	0.67	3.97	2.29	0.43	1.01	70.92
BR16	26.10	red mudstone	11.67	0.20	0.59	3.88	2.05	0.29	1.15	72.65
BR15	24.10	light grey mudstone	11.16	0.26	/	3.34	2.29	0.18	0.9	/
BR14	22.10	light grey mudstone	10.78	0.21	1.30	3.28	1.92	0.23	1.21	65.89
BR13	20.10	light grey mudstone	11.95	0.24	/	3.43	1.94	0.14	0.75	/
BR12	18.10	light grey mudstone	11.61	0.26	0.84	3.39	2.27	0.16	1.01	71.63

BR11	15.10	light grey mudstone	11.51	0.21	0.75	3.29	1.96	0.13	1.15	72.81
BR10	13.10	light grey mudstone	11.66	0.53	0.91	4.38	2.33	0.46	1.39	67.86
BR9	11.60	light grey mudstone	11.33	0.25	0.68	3.48	2.11	0.36	0.87	72.54
BR8	10.10	light grey mudstone	10.27	0.49	1.14	3.19	1.87	0.13	1.57	66.6
BR7	8.60	light grey mudstone	10.77	0.26	0.81	3.51	2.06	0.37	1.53	70
BR6	7.10	light grey mudstone	11.29	0.19	0.68	3.45	2.27	0.12	1.28	72.53
BR5	5.60	light grey mudstone	11.91	0.25	0.81	3.86	2.24	0.59	0.97	70.88
BR4	3.50	light grey mudstone	11.59	0.20	0.61	3.61	2.19	0.17	1.36	73.25
BR3	3.00	light grey mudstone	11.88	0.20	0.94	3.72	2.29	0.12	1.3	70.06
BR2	1.50	grey-green mudstone	11.01	0.28	0.67	3.28	2.32	0.1	1.62	72.85
BR1	0.00	grey-green mudstone	10.27	0.22	0.71	3.33	2.04	0.13	1.15	70.77

Table S3. Organic C and pyrite S isotopes, and Fe speciation contents, in Ashgill Beck samples, Lake District, UK.

Name	Height (m)	Lithofacies Description	$\delta^{13}C_{org}$ (‰)	TOC (wt%)	$\delta^{34}S_{py}$ (‰)	Fe_T (wt%)	Fe_{carb} (wt%)	Fe_{ox} (wt%)	Fe_{mag} (wt%)	Fe_{py} (wt%)	Fe_{HR}/Fe_T	Fe_{py}/Fe_{HR}
AG50	64.50	finely laminated, medium grey mudstone	-28.09	0.35	-21.88	4.20	0.52	0.07	0.04	0.96	0.38	0.61
AG49	62.70	finely laminated, medium grey mudstone	-27.85	0.35	-21.54	4.25	0.51	0.04	0.05	0.93	0.36	0.60
AG48	61.20	finely laminated, medium grey mudstone	-27.79	0.38	-22.17	4.27	0.45	0.20	0.07	0.68	0.33	0.49
AG47	59.20	finely laminated, medium grey mudstone	-27.79	0.41	-21.66	4.41	0.64	0.45	0.05	0.65	0.40	0.36
AG46	58.00	finely laminated, medium grey mudstone	-28.55	0.39	-22.37	4.68	0.50	0.04	0.03	1.18	0.37	0.67
AG45	56.10	finely laminated, medium grey mudstone	-27.72	0.39	-22.19	4.37	0.53	0.13	0.05	0.89	0.36	0.56
AG44	54.70	finely laminated, medium grey mudstone	-28.03	0.36	-20.67	4.30	0.42	0.04	0.05	1.01	0.35	0.66
AG43	53.20	finely laminated, medium grey mudstone	-27.91	0.36	-20.86	4.32	0.31	0.24	0.03	0.59	0.27	0.50
AG42	51.40	finely laminated, medium grey mudstone	-27.49	0.52	-16.30	3.73	0.32	0.50	0.10	0.06	0.26	0.06
AG41	49.80	finely laminated, medium grey mudstone	-27.42	0.48	-20.73	4.54	0.41	0.07	0.07	0.95	0.33	0.64
AG40	48.25	finely laminated, medium grey mudstone	-27.56	0.44	-21.24	4.69	0.47	0.32	0.06	0.83	0.36	0.49
AG39	46.80	finely laminated, medium grey mudstone	-27.45	0.44	-20.00	4.42	0.45	0.05	0.07	1.02	0.36	0.64
AG38	44.10	finely laminated, medium grey mudstone	-27.84	0.43	-20.71	4.43	0.41	0.05	0.04	0.95	0.33	0.65
AG37	42.00	finely laminated, medium grey mudstone	-27.60	0.47	-21.49	4.48	0.45	0.22	0.06	0.54	0.28	0.43
AG36	40.20	finely laminated, medium grey mudstone	-27.37	0.49	-18.98	4.44	0.48	0.16	0.06	0.87	0.35	0.56
AG35	38.80	very finely laminated, dark grey mudstone	-27.09	0.58	-18.81	4.31	0.39	0.16	0.06	0.80	0.33	0.56
AG34	37.30	very finely laminated, dark grey mudstone	-27.50	0.52	-21.04	4.73	0.49	0.26	0.05	0.92	0.36	0.54
AG33	35.50	very finely laminated, dark grey mudstone	-27.27	0.51	-20.40	4.60	0.42	0.28	0.07	0.74	0.33	0.49
AG32	34.20	very finely laminated, dark grey mudstone	-26.50	0.73	-19.08	4.29	0.49	0.30	0.04	1.00	0.42	0.55
AG31	32.90	very finely laminated, dark grey mudstone	-26.47	0.56	-15.45	4.61	0.51	0.09	0.05	1.05	0.37	0.62
AG30	30.40	very finely laminated, dark grey mudstone	-26.56	0.75	-17.06	5.08	0.43	0.48	0.05	1.15	0.42	0.55
AG29	29.30	very finely laminated, dark grey mudstone	-26.26	0.69	-14.21	4.43	0.34	0.57	0.07	0.50	0.33	0.34

AG28	28.25	very finely laminated, dark grey mudstone	-26.28	0.64	-18.04	4.84	0.43	0.33	0.05	0.94	0.36	0.53
AG27	27.30	very finely laminated, dark grey mudstone	-26.58	0.60	-15.68	4.72	0.52	0.38	0.07	1.03	0.43	0.51
AG26	25.87	very finely laminated, dark grey mudstone	-26.15	0.54	-16.82	4.76	0.41	0.22	0.06	0.73	0.30	0.51
AG25	24.70	very finely laminated, dark grey mudstone	-26.53	0.74	-18.57	4.73	0.45	0.20	0.05	1.14	0.39	0.62
AG24	23.80	very finely laminated, dark grey mudstone	-26.16	0.64	-18.72	4.81	0.47	0.79	0.06	0.59	0.40	0.31
AG23	22.60	very finely laminated, dark grey mudstone	-25.88	0.99	-15.28	4.84	0.30	0.78	0.07	0.55	0.35	0.33
AG22	21.50	very finely laminated, dark grey mudstone	-26.04	0.71	-13.91	4.49	0.43	0.38	0.03	1.27	0.47	0.60
AG21	20.51	very finely laminated, dark grey mudstone	-26.22	0.63	-13.24	4.36	0.52	0.13	0.06	1.00	0.39	0.59
AG20	19.40	very finely laminated, dark grey mudstone	-26.17	0.83	-14.11	4.58	0.45	0.41	0.03	0.95	0.40	0.52
AG19	18.20	very finely laminated, dark grey mudstone	-26.36	0.60	-16.19	4.60	0.45	0.23	0.05	0.94	0.36	0.56
AG18	16.80	very finely laminated, dark grey mudstone	-26.54	0.67	-16.77	4.69	0.47	0.30	0.07	0.80	0.35	0.49
AG17	15.30	very finely laminated, dark grey mudstone	-26.23	0.56	-16.17	4.65	0.42	0.23	0.07	0.95	0.36	0.57
AG16	14.30	very finely laminated, dark grey mudstone	-26.54	0.73	-17.52	4.70	0.48	0.36	0.06	0.93	0.39	0.51
AG15	13.50	very finely laminated, dark grey mudstone	-26.29	0.74	-16.32	4.90	0.36	0.65	0.14	0.42	0.32	0.27
AG14	12.30	very finely laminated, dark grey mudstone	-26.25	0.73	-14.55	4.51	0.44	0.54	0.06	0.60	0.36	0.37
AG13	11.20	very finely laminated, dark grey mudstone	-26.22	0.63	-13.74	4.23	0.45	0.28	0.06	0.54	0.31	0.41
AG12	10.10	very finely laminated, dark grey mudstone	-26.86	0.54	-17.35	4.07	0.48	0.17	0.07	0.84	0.38	0.54
AG11	8.90	very finely laminated, dark grey mudstone	-26.55	0.54	-18.44	4.26	0.39	0.14	0.03	0.92	0.35	0.62
AG10	7.62	very finely laminated, dark grey mudstone	-26.55	0.48	-17.60	4.30	0.48	0.06	0.06	0.87	0.34	0.59
AG9	6.13	very finely laminated, dark grey mudstone	-26.84	0.53	-17.20	4.23	0.49	0.32	0.07	0.67	0.37	0.43
AG8	4.86	very finely laminated, dark grey mudstone	-27.12	0.57	-15.55	4.63	0.52	0.31	0.06	0.79	0.36	0.47
AG7	4.36	very finely laminated, dark grey mudstone	-27.28	0.46	-20.45	4.83	0.42	0.07	0.06	1.17	0.35	0.68
AG6	4.10	very finely laminated, dark grey mudstone	-27.16	0.43	-20.29	4.77	0.24	0.05	0.06	1.13	0.31	0.76
AG5	4.00	very finely laminated, dark grey mudstone	-27.10	0.41	-22.24	4.59	0.24	0.03	0.07	1.11	0.32	0.77
AG4	3.25	light grey mudstone	-27.62	0.12	/	4.52	0.30	0.20	0.16	0.00	0.15	0.00
AG3	2.63	light grey mudstone	-27.30	0.08	-29.20	5.53	0.22	0.10	0.09	0.05	0.08	0.11

AG2	1.65	light grey mudstone	-27.63	0.25	/	4.86	0.24	0.08	0.10	0.00	0.09	0.01
AG1	0.00	light grey mudstone	-27.79	0.15	-29.10	5.08	0.18	0.03	0.09	0.00	0.06	0.01

Table S4. Major and trace element compositions of Ashgill Beck samples, Lake District, UK.

Name	Height (m)	Lithofacies Description	Al (wt%)	Ca (wt%)	Na (wt%)	K (wt%)	U (ppm)	Mo (ppm)	Re (ppb)
AG50	64.50	finely laminated, medium grey mudstone	7.66	3.40	1.13	2.60	3.67	5.50	7.36
AG49	62.70	finely laminated, medium grey mudstone	8.15	2.75	1.15	2.82	3.71	5.32	7.27
AG48	61.20	finely laminated, medium grey mudstone	8.43	0.99	1.13	2.92	3.80	7.08	8.02
AG47	59.20	finely laminated, medium grey mudstone	8.43	0.84	1.10	2.87	3.67	9.45	8.30
AG46	58.00	finely laminated, medium grey mudstone	8.93	0.44	1.14	3.07	3.95	5.97	7.63
AG45	56.10	finely laminated, medium grey mudstone	8.24	2.01	1.10	2.78	3.71	6.35	8.28
AG44	54.70	finely laminated, medium grey mudstone	8.23	3.28	1.06	2.77	3.46	5.98	7.36
AG43	53.20	finely laminated, medium grey mudstone	9.12	0.19	1.03	3.05	3.63	4.72	7.29
AG42	51.40	finely laminated, medium grey mudstone	9.53	0.19	1.25	3.27	3.65	1.41	12.35
AG41	49.80	finely laminated, medium grey mudstone	9.23	0.22	1.19	3.05	3.91	5.00	7.30
AG40	48.25	finely laminated, medium grey mudstone	8.61	1.14	1.13	2.84	3.32	4.66	7.53
AG39	46.80	finely laminated, medium grey mudstone	9.15	0.72	1.16	3.12	3.76	6.04	8.02
AG38	44.10	finely laminated, medium grey mudstone	9.13	1.50	1.18	2.97	3.75	5.46	7.20
AG37	42.00	finely laminated, medium grey mudstone	8.70	0.80	1.14	2.84	3.34	5.07	6.99
AG36	40.20	finely laminated, medium grey mudstone	8.91	1.52	1.19	2.97	3.76	5.42	7.41
AG35	38.80	very finely laminated, dark grey mudstone	9.14	2.60	1.12	3.09	2.38	1.01	2.54
AG34	37.30	very finely laminated, dark grey mudstone	8.55	1.11	1.18	2.77	3.50	5.44	8.16
AG33	35.50	very finely laminated, dark grey mudstone	9.25	0.19	1.19	2.99	3.84	6.08	8.34
AG32	34.20	very finely laminated, dark grey mudstone	7.97	3.10	0.97	2.68	2.82	2.00	4.99
AG31	32.90	very finely laminated, dark grey mudstone	8.34	1.23	1.07	2.69	2.55	1.97	5.71
AG30	30.40	very finely laminated, dark grey mudstone	8.86	0.52	1.15	2.85	2.95	4.20	7.67
AG29	29.30	very finely laminated, dark grey mudstone	8.66	1.60	1.00	2.93	2.78	2.08	4.33

AG28	28.25	very finely laminated, dark grey mudstone	8.55	1.23	1.11	2.73	2.85	2.63	6.45
AG27	27.30	very finely laminated, dark grey mudstone	8.06	2.74	1.04	2.61	2.80	3.49	6.53
AG26	25.87	very finely laminated, dark grey mudstone	9.17	2.44	1.24	3.00	3.18	4.75	8.00
AG25	24.70	very finely laminated, dark grey mudstone	8.63	0.88	1.09	2.79	3.40	4.96	8.63
AG24	23.80	very finely laminated, dark grey mudstone	8.73	2.37	1.01	2.97	3.11	4.44	6.76
AG23	22.60	very finely laminated, dark grey mudstone	9.29	0.15	1.02	3.14	3.02	2.95	4.96
AG22	21.50	very finely laminated, dark grey mudstone	8.51	2.05	0.97	3.05	2.81	2.88	3.86
AG21	20.51	very finely laminated, dark grey mudstone	7.86	4.25	0.84	2.70	2.58	2.43	3.74
AG20	19.40	very finely laminated, dark grey mudstone	8.33	0.74	1.00	2.79	2.88	2.73	4.41
AG19	18.20	very finely laminated, dark grey mudstone	8.37	2.06	1.01	2.81	2.90	2.66	4.71
AG18	16.80	very finely laminated, dark grey mudstone	8.62	1.68	0.98	2.82	2.70	2.32	4.96
AG17	15.30	very finely laminated, dark grey mudstone	8.49	2.04	0.98	2.88	2.76	3.30	5.24
AG16	14.30	very finely laminated, dark grey mudstone	8.44	1.15	1.02	2.81	2.88	3.56	5.35
AG15	13.50	very finely laminated, dark grey mudstone	8.99	0.17	1.05	3.04	2.77	2.68	4.38
AG14	12.30	very finely laminated, dark grey mudstone	8.48	1.33	0.92	2.95	2.28	1.90	3.06
AG13	11.20	very finely laminated, dark grey mudstone	8.10	3.19	0.94	2.84	2.24	1.91	2.53
AG12	10.10	very finely laminated, dark grey mudstone	8.16	3.34	0.92	2.88	2.63	2.09	3.57
AG11	8.90	very finely laminated, dark grey mudstone	7.83	3.93	0.89	2.74	2.82	2.53	3.36
AG10	7.62	very finely laminated, dark grey mudstone	7.95	3.98	0.89	2.75	2.39	2.07	3.09
AG9	6.13	very finely laminated, dark grey mudstone	7.41	3.46	0.82	2.65	2.22	1.71	2.54
AG8	4.86	very finely laminated, dark grey mudstone	8.06	2.76	0.64	2.98	2.38	3.08	2.02
AG7	4.36	very finely laminated, dark grey mudstone	8.40	0.87	0.78	3.05	3.02	3.13	3.69
AG6	4.10	very finely laminated, dark grey mudstone	8.60	0.59	0.83	3.12	3.05	1.34	3.03
AG5	4.00	very finely laminated, dark grey mudstone	9.84	0.77	1.10	3.41	3.20	0.38	1.61
AG4	3.25	light grey mudstone	8.90	0.42	0.89	3.41	3.04	1.19	3.08
AG3	2.63	light grey mudstone	8.88	0.18	0.98	2.83	2.03	0.15	1.47

AG2	1.65	light grey mudstone	8.79	0.76	1.05	2.94	2.45	0.62	1.65
AG1	0.00	light grey mudstone	9.40	2.22	1.02	3.18	1.88	0.05	1.18

Table S5. Detailed geochemical information for U and Mo isotope samples in the Banwy River section and Ashgill Beck section, UK.

Name	Section	Depth	TOC (wt%)	Fe_{HR}/Fe_T	Fe_{py}/Fe_{HR}	Re (ppb)	U (ppm)	Mo (ppm)	$\delta^{238}U$ (‰)	2 s.e. (‰)	$\delta^{98}Mo$ (‰)	2 s.e. (‰)	Redox interpretation
BR145	BR	185.39	0.69	0.48	0.47	5.21	3.17	2.69	-0.35	0.07	0.45	0.03	ferruginous
BR141	BR	181.19	0.59	0.43	0.47	5.82	3.35	2.51	-0.30	0.06	0.10	0.03	ferruginous
BR137	BR	176.69	0.76	0.49	0.49	3.52	2.75	2.59	-0.32	0.06	-1.29	0.07	ferruginous
BR135	BR	174.49	0.61	0.52	0.52	4.63	3.07	2.60	-0.32	0.06	0.44	0.03	ferruginous
BR132	BR	171.09	0.57	0.55	0.54	4.80	3.15	4.65	-0.36	0.06	0.95	0.04	ferruginous
BR128	BR	166.39	0.59	0.44	0.51	4.25	3.19	2.57	-0.26	0.06	0.08	0.04	ferruginous
BR124	BR	161.99	0.65	0.45	0.50	4.17	3.13	1.91	-0.32	0.07	0.26	0.04	ferruginous
BR122	BR	159.89	0.80	0.53	0.54	5.70	3.34	5.18	-0.23	0.06	0.50	0.03	weakly euxinic
BR110	BR	156.49	0.72	0.46	0.61	3.52	2.51	2.88	-0.33	0.06	0.76	0.03	weakly euxinic
BR107	BR	150.49	0.79	0.44	0.63	4.16	2.93	3.99	-0.28	0.05	0.48	0.03	weakly euxinic
BR106	BR	148.84	0.60	0.40	0.60	3.89	2.14	1.48	-0.30	0.06	-0.21	0.02	weakly euxinic
BR104	BR	145.84	0.76	0.41	0.68	4.43	3.39	3.62	-0.30	0.05	0.40	0.04	weakly euxinic
BR103	BR	144.74	0.64	0.60	0.79	3.53	2.50	2.31	-0.31	0.07	0.14	0.05	weakly euxinic
BR101	BR	141.29	0.78	0.41	0.64	4.33	2.54	2.75	-0.25	0.06	0.13	0.04	weakly euxinic
BR98	BR	137.29	0.72	0.45	0.62	3.67	2.37	2.56	-0.33	0.07	0.90	0.05	weakly euxinic
BR95	BR	133.69	0.65	0.45	0.65	3.86	2.62	3.45	-0.23	0.08	0.42	0.03	weakly euxinic
BR90	BR	127.98	0.60	0.42	0.61	2.34	2.36	2.84	-0.29	0.06	0.08	0.04	weakly euxinic
BR71	BR	106.93	0.29	0.19	0.20	1.55	2.23	1.29	-0.30	0.06	0.60	0.04	ferruginous
BR53	BR	95.83	0.38	0.17	0.24	3.48	2.32	1.55	-0.28	0.05	0.45	0.03	ferruginous
BR43	BR	78.72	0.10	0.11	0.11	1.17	2.37	0.48	-0.36	0.06	/	/	dysoxic
BR38	BR	68.03	0.12	0.10	0.01	1.22	1.71	0.14	-0.35	0.06	/	/	dysoxic
BR25	BR	42.8	0.10	0.27	0.00	0.86	2.28	0.49	-0.34	0.07	-1.52	0.04	oxic

BR22	BR	38.2	0.13	0.29	0.00	1.25	2.14	0.46	-0.33	0.07	-1.54	0.05	oxic
BR17	BR	28.1	0.13	0.26	0.00	1.01	2.29	0.43	-0.40	0.07	-1.44	0.06	oxic
BR12	BR	18.1	0.08	0.08	0.01	1.01	2.27	0.16	-0.34	0.06	/	/	dysoxic
BR9	BR	11.6	0.11	0.11	0.01	0.87	2.11	0.36	-0.31	0.06	-2.39	0.04	dysoxic
BR6	BR	7.1	0.10	0.08	0.02	1.28	2.27	0.12	-0.31	0.07	/	/	dysoxic
AG50	AB	64.5	0.35	0.38	0.61	7.36	3.67	5.50	-0.18	0.05	0.24	0.08	weakly euxinic
AG48	AB	61.2	0.38	0.33	0.49	8.02	3.80	7.08	-0.20	0.05	0.49	0.08	ferruginous
AG42	AB	51.4	0.52	0.26	0.06	12.35	3.65	1.41	-0.19	0.05	-0.61	0.08	ferruginous
AG37	AB	42	0.47	0.28	0.43	6.99	3.34	5.07	-0.30	0.05	0.63	0.04	ferruginous
AG33	AB	35.5	0.51	0.33	0.49	8.34	3.84	6.08	-0.24	0.06	0.61	0.04	ferruginous
AG30	AB	30.4	0.75	0.42	0.55	7.67	2.95	4.20	-0.35	0.06	0.86	0.03	weakly euxinic
AG28	AB	28.25	0.64	0.36	0.53	6.45	2.85	2.63	-0.29	0.05	0.47	0.03	ferruginous
AG25	AB	24.7	0.74	0.39	0.62	8.63	3.40	4.96	-0.25	0.06	0.39	0.03	weakly euxinic
AG21	AB	20.51	0.63	0.39	0.59	3.74	2.58	2.43	-0.34	0.05	0.52	0.04	weakly euxinic
AG18	AB	16.8	0.67	0.35	0.49	4.96	2.70	2.32	-0.25	0.05	0.33	0.04	ferruginous
AG16	AB	14.3	0.73	0.39	0.51	5.35	2.88	3.56	-0.21	0.07	0.60	0.05	weakly euxinic
AG9	AB	6.13	0.53	0.37	0.43	2.54	2.22	1.71	-0.32	0.05	-0.20	0.05	ferruginous
AG4	AB	3.25	0.12	0.15	0.00	3.08	3.04	1.19	-0.32	0.06	/	0.12	ferruginous
AG2	AB	1.65	0.25	0.09	0.01	1.65	2.45	0.62	-0.25	0.07	0.21	0.07	ferruginous

Table S6. Parameters used in the U-Mo mass balance model.

Parameter	U	Mo	Reference
A_0	3.6×10^{14} m^2		*(106)*
$A_{euxinic0}$	0.0011		*(80)*
$A_{ferruginous0}$	0.0192		*(80)*
$A_{(dys)oxic0}$	$1\text{-}A_{euxinic0}\text{-}A_{ferruginous0}$		Mass balance
[Me]	1.9×10^{13} mol	1.35×10^{14} mol	*(106, 61)*
δ_{SW}	-0.39‰	2.34‰	*(107, 61)*
F_{river}	$(27.5 – 56.5) \times 10^6$ mol yr^{-1}	$(18 - 30) \times 10^7$ mol yr^{-1}	*(108, 109)*
δ_{river}	-0.24 ~ -0.34‰	0.5 ~ 0.9‰	*(110, 61)*
$F_{euxinic0}$	5×10^6 mol yr^{-1}	4.6×10^7 mol yr^{-1}	*(61)*
$F_{ferruginous0}$	15×10^6 mol yr^{-1}	15.5×10^7 mol yr^{-1}	*(61)*
$F_{(dys)oxic0}$	22×10^6 mol yr^{-1}	10.9×10^7 mol yr^{-1}	*(61)*
$\Delta_{euxinic}$	0.4 ~ 0.85‰	0 to –0.5‰	*(110, 61)*
$\Delta_{ferruginous}$	0.1 ~ 0.4‰	–2 to –0.5‰	*(111, 112)*
Δ_{oxic}	-0.2 ~ 0‰	–3 to –2 ‰	*(61)*